Statistical characteristics of the SOL turbulence in the first divertor plasma operation of W7-X using a reciprocating probe

S. C. Liu, Y. Liang, H. Q. Wang, et al.

View Online **Export Citation** **CrossMark**
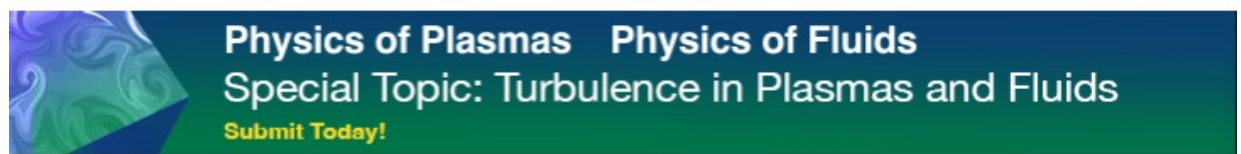
ARTICLES YOU MAY BE INTERESTED IN

Internal measurement of magnetic turbulence in ELMy H-mode tokamak plasmas
Physics of Plasmas 27, 120701 (2020); https://doi.org/10.1063/5.0029996

Blob interactions in 2D scrape-off layer simulations
Physics of Plasmas 27, 122301 (2020); https://doi.org/10.1063/5.0021314

Characteristics of the SOL turbulence structure in the first experimental campaign on W7-X with limiter configuration
Physics of Plasmas 25, 072502 (2018); https://doi.org/10.1063/1.5033353

Physics of Plasmas   Physics of Fluids
Special Topic: Turbulence in Plasmas and Fluids
Submit Today!

AIP Publishing

Statistical characteristics of the SOL turbulence in the first divertor plasma operation of W7-X using a reciprocating probe

S. C. Liu,[1,2,a] (iD) Y. Liang,[1,2,a] (iD) H. Q. Wang,[1] (iD) C. Killer,[3] (iD) P. Drews,[2] (iD) A. Knieps,[2] (iD) X. Han,[1,2] (iD) O. Grulke,[3]
A. Krämer-Flecken,[2] (iD) G. S. Xu,[1] (iD) N. Yan,[1] D. Höschen,[2] D. Nicolai,[2] (iD) G. Satheeswaran,[2] (iD) J. Geiger,[3] M. Henkel,[2]
Z. Huang,[2] R. König,[3] Y. Li,[1,2] (iD) O. Neubauer,[2] K. Rahbarnia,[3] N. Sandri,[2] B. Schweer,[2] (iD) E. H. Wang,[1,2]
Y. M. Wang,[1] (iD) S. Xu,[1,2] X. Gao,[1] (iD) and W7-X Team[b]

AFFILIATIONS

[1]Institute of Plasma Physics, Chinese Academy of Sciences, Hefei 230031, People's Republic of China
[2]Institut für Energie- und Klimaforschung–Plasmaphysik, Partner of the Trilateral Euregio Cluster (TEC), Forschungszentrum Jülich
  GmbH, 52425 Jülich, Germany
[3]Max-Planck-Institute for Plasma Physics, 17491 Greifswald, Germany

[a]**Authors to whom correspondence should be addressed:** shaocheng.liu@ipp.ac.cn and y.liang@fz-juelich.de
[b]The W7-X team is listed in the paper [Klinger *et al.*, Nucl. Fusion **59**, 112004 (2019)].

ABSTRACT

The statistical characteristics of the scrape-off layer (SOL) turbulence have been investigated in the first divertor plasma operation of W7-X using a reciprocating probe. The turbulence spectra, auto-correlation time and the statistical parameters are analyzed in three magnetic configurations. In standard and high mirror configurations, the SOL turbulence can be classified into four patterns from the outer SOL to the inner SOL, and each pattern is characterized by the poloidal cross correlation spectrum and the turbulence propagation property. A strong dependence of the SOL turbulence on the magnetic topology is demonstrated experimentally. In high iota configuration, the SOL island is relatively narrow and consequently the fluctuation level of turbulence is weak in the far SOL but enhanced significantly in the near SOL. In the reversed field case, the SOL turbulence reveals similar propagation properties and statistical parameters with those in the normal field case, demonstrating the same turbulence structure in both toroidal field directions.

Published under license by AIP Publishing. https://doi.org/10.1063/5.0016151

I. INTRODUCTION

Turbulence plays an important role in the plasma instability and transport in the magnetic controlled fusion devices.[1] The anomalous transport which is considered to be driven by the drift wave turbulence dominates the edge cross field transport.[2] Turbulence induced transport is closely related to the gradient of plasma density, temperature and radial electric field shear.[3] According to the free energy source, turbulence can be classified into some groups which are characterized by some important parameters, such as fluctuation levels of plasma density and temperature, propagation speed and direction, frequency range and wave number.[3] Consequently, the study of edge and scrape-off layer (SOL) turbulence characteristics is of great benefit to the understanding of edge plasma transport. Usually the edge and SOL turbulence is measured by some diagnostics, such as Langmuir probe,[4] reflectometry,[5] gas puff imaging,[6] and beam emission spectroscopy.[7]

In Wendelstein 7-X (W7-X), the SOL turbulence has been measured by reciprocating probes and reflectometry.[8,9] Since W7-X is a stellarator with inherent three-dimensional magnetic topology, the SOL turbulence structure exhibits strong topology dependence. In the limiter configuration of W7-X, an electromagnetic coherent mode is observed in the SOL magnetic island and enhanced in the configuration with long connection length.[8] In the divertor configuration, the SOL plasma profiles are affected significantly by the divertor configurations, including the electron temperature, density, electric field, and parallel flow.[10,11] As measured by the reflectometry, a quasi-coherent mode near the plasma edge appears in the standard divertor configuration but disappears in the high iota configuration on W7-X.[12] The SOL turbulence transport exhibits two distinct transport patterns: a broadband turbulence dominant region in the outer SOL and a low frequency dominant region in the inner SOL.[13] In our previous work,

the SOL turbulence properties in the limiter configuration have been analyzed systematically, including the fluctuation level, probability density function, auto-correlation time, turbulence correlation length, phase velocity, and poloidal power spectra.[14] In this paper, the statistical characteristics of the SOL turbulence in the first divertor experimental campaign (OP 1.2a) of W7-X will be presented. The rest of the paper is organized as follows. The experimental setup is described in Sec. II. The characterization of the SOL turbulence in standard configuration is presented in Sec. III. The SOL turbulence characterization in high mirror configuration and high iota configuration is given in Secs. IV and V, respectively. Section VI is the summary.

II. EXPERIMENTAL SETUP

W7-X, a new optimized stellarator with a major radius of 5.5 m and a minor radius of $\sim$0.5 m,[15] is equipped with 50 nonplanar coils and 20 planar coils to accommodate flexible magnetic configurations.[16] The rotational transform iota is defined as $\iota/2\pi = n/m$, where m is the poloidal mode and n is the toroidal mode. In the first divertor experimental campaign, there are three divertor configurations, including the high mirror configuration (KJM + 252) with an $\iota/2\pi = 5/5$ island chain in the SOL, the standard divertor configuration (EJM + 252 and EJM-252) with an $\iota/2\pi = 5/5$ island chain, and high iota configuration (FTM + 252) with an $\iota/2\pi = 5/4$ island chain. Note that the sign in the definition of configuration name denotes the direction of the toroidal magnetic field, with positive sign in the anti-clockwise direction viewed from top, and the negative sign in the clockwise direction. The Poincaré plot in the poloidal plane of the reciprocating probe is shown in Fig. 1 for the three divertor configurations in OP 1.2a. It should be pointed out that the Poincaré plot and the field line connection length along the probe path are derived from the field line tracer of W7-X by using the real coil settings, and the uncertainty of the magnetic equilibrium could be up to 1 cm.[17–19] In the calculation of connection length, all the components of the first wall on W7-X in OP 1.2a are taken into account. The connection length has a sharp increase at the outer boundary of the island, keeps almost constant inside the island, then increases quickly again in the near SOL and finally reaches the upper limit. As illustrated in Fig. 1,

the width of the magnetic island in high mirror and standard configurations is much larger than that in high iota configuration. Along the probe path, the island with clear nested field lines is located in the radial region $R = 6.022$–6.078 m for high mirror configuration, 6.036–6.096 m for standard configuration, and 6.014–6.036 m for high iota configuration. The last closed flux surface (LCFS), as shown in the black line in Fig. 1, is about $R = 6.005$, 6.027, and 6.001 m for the KJM + 252, EJM + 252, and FTM + 252 configurations, respectively.

The multiple-purpose manipulator (MPM) has been developed and operated on W7-X since 2015, which is located under the outer midplane with vertical coordinate $Z = -167$ mm.[20,21] The temporal resolution of MPM is 2 MHz. The layout of the probe head (FZJ-COMB2) used in our experiment is illustrated in Figs. 1 and 2. The front surface of probe head is designed to align the local flux surface, therefore the plasma parameters and turbulence information on the same flux surface can be obtained. In Fig. 2(b), the pins measuring the floating potential are ϕ_{f1}, ϕ_{f2}, ϕ_{f3}, ϕ_{f4}, and ϕ_{f5}. The two pins ϕ_{f3} and ϕ_{f4} are on the top plateau which is 3.8 mm higher than the other three floating potential pins. The double probe consists of I_s and ϕ_+, with a biasing voltage of 286 V. Note that all the pins measuring floating potential have a diameter of 1.4 mm, while the pins of the double probe have a diameter of 2 mm. All the pins have the same length of 3 mm. With the setup of the Langmuir probe pins, it is able the study the turbulence poloidal structure through ϕ_{f1}, ϕ_{f2} and ϕ_{f5} or ϕ_{f3}, and ϕ_{f4}. In order to minimized the block effect between probe pins, every pin has a gap ($\sim$1 mm) with its adjacent pin along the poloidal direction. In addition, as illustrated in Fig. 2(a), the middle plateau is shaped as a rectangle and 3.5 mm higher than the lowest plateau, which also can minimize the block effect due to the probe boron nitride cover when the magnetic field line has a small angle with the front surface plane.

In this paper, four discharges with deep probe plunge are analyzed to characterize the SOL turbulence, with plasma program #20171026.38 in EJM + 252 (standard) configuration, #20171207.49 in EJM-252 (standard) configuration, #20171017.47 in KJM + 252 (high mirror) configuration and #20171025.35 in FTM + 252 (high iota) configuration. The plasma parameters of three discharges are
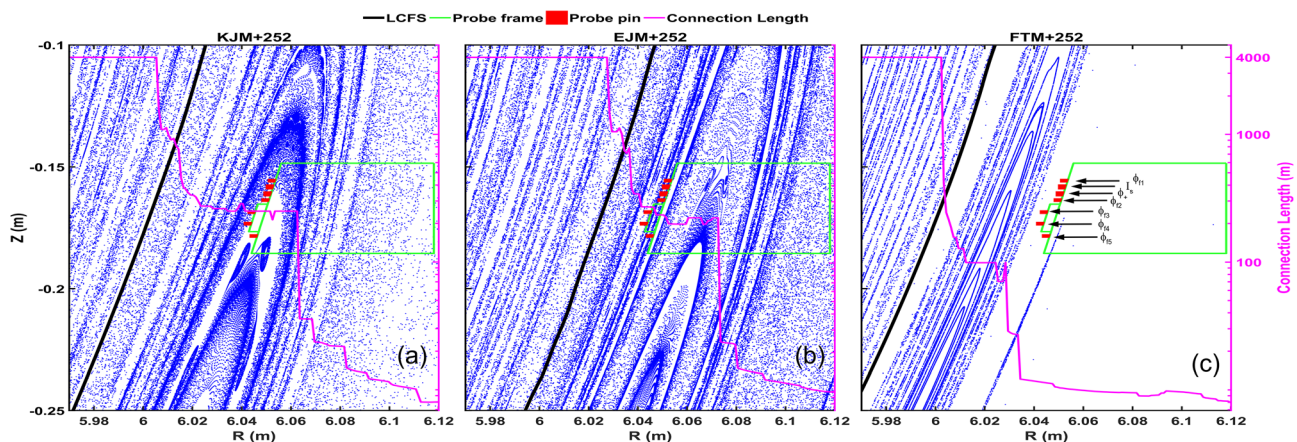

FIG. 1. The Poincaré plot of the three divertor configurations in OP1.2a. From left to right, they are the high mirror configuration (a), standard divertor configuration (b), and the high iota configuration (c), respectively. The probe frame is shown in green and the probe pins are highlighted in red, and the physics name of each pin is labeled in (c). The connection length is shown in the magenta line.
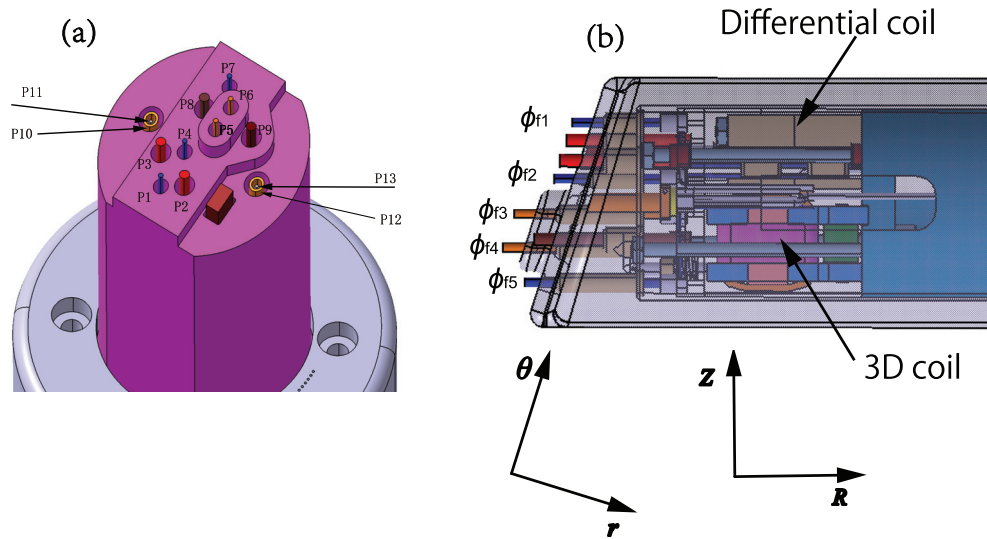
FIG. 2. The arrangement of the FZJ-COMB2 probe head. (a) Sketch of probe pins; (b) side view of probe head.

illustrated in Fig. 3. During the probe plunge, the electron cyclotron resonance heating (ECRH) power and plasma stored energy are almost constant, indicating stable plasma conditions. As calculated by the field line tracer and demonstrated by experiments, the toroidal plasma current reveals a significant impact on the edge magnetic topology.[10,11] As illustrated in Fig. 3(c), the changes of plasma current

FIG. 3. Plasma parameters of three discharges used in this paper. (a) ECRH heating power; (b) plasma stored energy; (c) toroidal plasma current; (d) radial position of probe.

is very small during the probe plunge, and the induced topology variation can be ignored. In the calculation of field line connection length and Poincaré plot, the averaged plasma current during probe plunge is taken into account. Note that in discharge #20171207.49 the probe is plunged at 24 s, which is much longer than the pulse lengths of the other three, therefore its plasma parameters which are also stable during probe plunge are not shown in Fig. 3.

The SOL profiles measured by probe are illustrated in Fig. 4. The electron temperature and electron density are derived from the four-tip triple probe, with $T_e = [\phi_+ - (\phi_{f1} + \phi_{f2})/2]/\ln 2$ and $n_e = I_s/(0.49 e A_{eff}\sqrt{T_e/m_i})$,[22] where $A_{eff} = 12\,\mathrm{mm}^2$. With the increase in the field line connection length in the outer SOL, the electron temperature and density increase significantly. In the standard configuration, the island center along probe path is located around $R = 6.068$ m. The electron density is flat at the island center, exhibits a steep gradient at the inner side of the island center and reaches a plateau, then decreases slightly, finally increases gradually in the near SOL. The electron temperature peaks at the island center with a narrow plateau, then decreases gradually to the minimum at $R = 6.058$ m, finally increases again in the near SOL. In the radial region of $R = 6.037$–6.041 m and $R = 6.044$–6.046 m, the gradient of the electron temperature is large. In the high mirror configuration, the radial evolutions of the electron temperature and electron density are similar with those in the standard configuration, except that the profiles are wider in the high mirror configuration because of the wider island structure. When the ECRH heating power raises from 1 MW to 2.1 MW, the electron temperature increases two times around the island center, but the change of the electron density is small. In high iota configuration, the electron temperature and density increase monotonously with the decreasing R, and the SOL widths of them are much smaller than those in the other two configurations, which is consistent with the narrower plateau of the connection length. In addition, the connection length at the plateau is around 100 m in high iota configuration, however it is around 250 m in the standard and high mirror
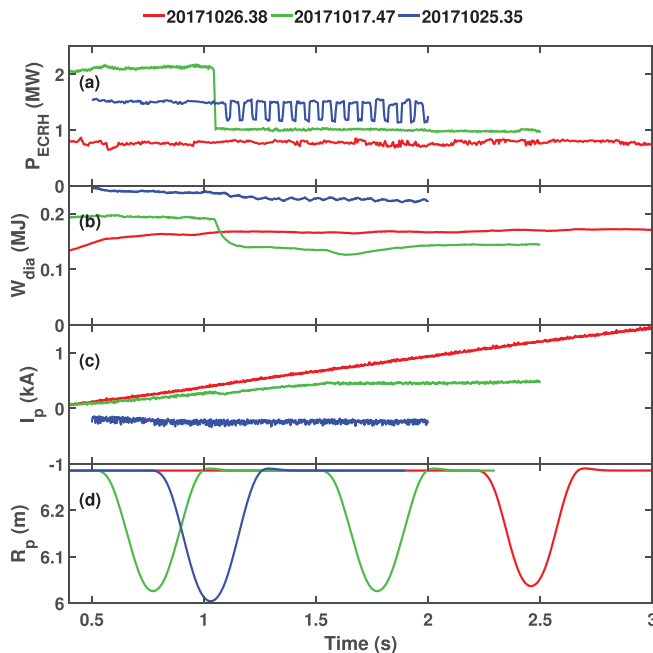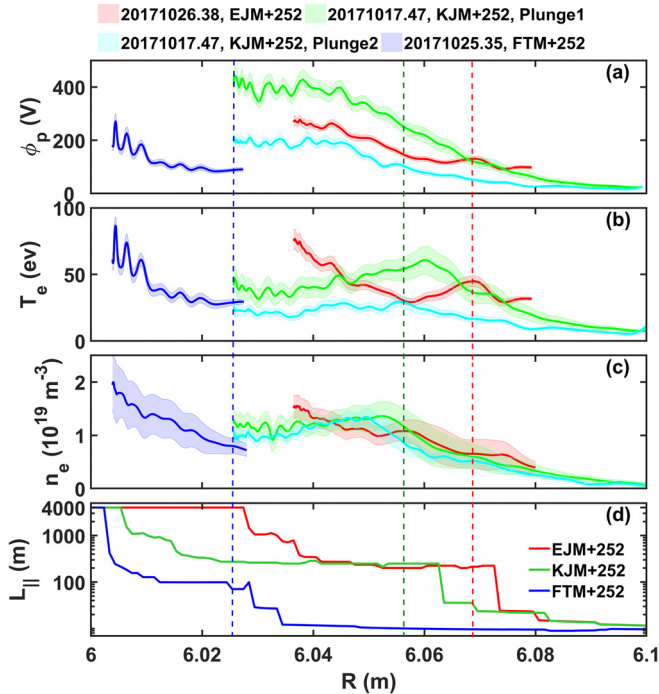
FIG. 4. The edge plasma profiles measured by the FZJ-COMB2 probe. (a) Plasma potential; (b) electron temperature; (c) electron density; (d) field line connection length. The shaded regions in (a)–(c) denote the standard deviation. The vertical dashed lines signify the location of the island center along the probe path for each configuration.
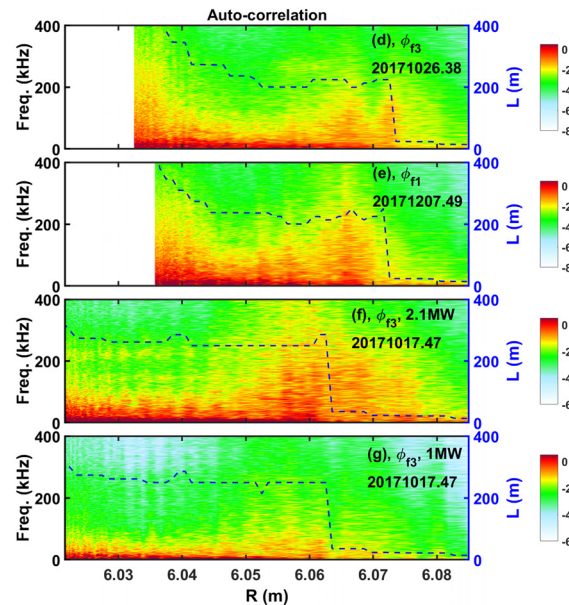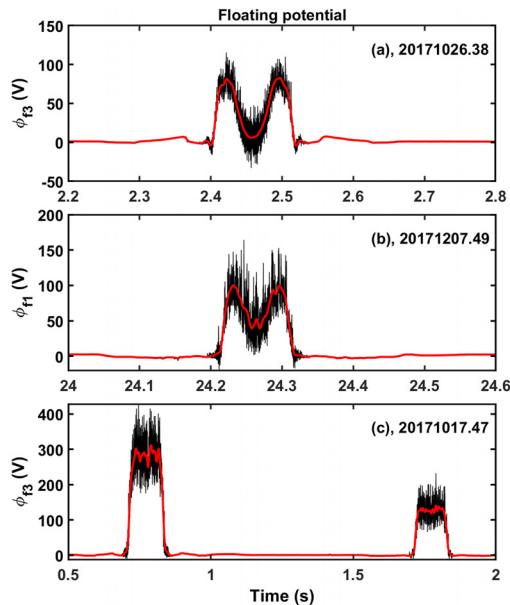
configurations. For the SOL profile measured in Fig. 4, the Debye length is about 0.02 mm, which is much smaller than the diameter of probe tip. The ion Larmor radius is smaller than 0.6 mm, which is shorter than the gap (1 mm) between two adjacent probe pins, indicating no block effect for the ion collection.

III. SOL TURBULENCE IN STANDARD DIVERTOR CONFIGURATION

A. Turbulence spectrum

In the standard configuration, two discharges with similar plasma parameters are chosen to illustrate the SOL turbulence structure, with the ECRH power of 1 MW. Plasma program #20171026.38 is in EJM + 252 configuration (B_t in anti-clockwise direction viewed from top, normal field), and the plasma program #20171207.49 is in EJM-252 configuration (B_t in clockwise direction, reversed field). As shown in Fig. 1, the LCFS is located at $R = 6.027$ m in standard configuration, and the innermost point of the probe is 5 mm outside the LCFS in the plasma program #20171026.38. The auto-power spectral density (APSD) of floating potential in standard and high mirror configurations are shown in Fig. 5. Here the APSD is calculated by $P_{xx}(\omega) = F_x^*(\omega)F_x(\omega)$, and $F_x(\omega)$ is the Fourier transform of signal $x(t)$.[23] Note that in Figs. 5 and 18, 2048 sample points ($\sim$1 ms) are used to calculate the discrete Fourier transform. The temporal evolution of floating potential is presented in Figs. 5(a) and 5(b), revealing the same radial variation between the plunge-in and plunge-out phases. In Figs. 5(d) and 5(e), the APSD increases sharply with the increasement of the connection length at the outer boundary of magnetic island. From the outer SOL to inner SOL, the intensive APSD is distributed in a wide frequency range (up to 200 kHz) at first, then is concentrated in low frequency range, and finally is distributed in a wide frequency range and its intensity decreases gradually with

FIG. 5. (a)–(c) Floating potential temporal evolution for standard and high mirror configurations; (d)–(g) auto-power spectral density of floating potential, and the field line connection length is illustrated in dashed lines. The plasma program and signal name are annotated in each panel.

frequency which follows the increasement of connection length in the inner SOL.

The cross correlation spectrum between two poloidally separated floating potential pins is shown in Fig. 6 for the standard configuration. The cross-power spectrum is calculated by $P_{xy}(\omega) = F_x^*(\omega)F_y(\omega) = |P_{xy}(\omega)|e^{i\alpha(\omega)}$, where $F_x(\omega)$ and $F_y(\omega)$ are the corresponding Fourier transform of signals $x(t)$ and $y(t)$, $|P_{xy}(\omega)|$ is the cross-power spectral density (CPSD), and $\alpha(\omega)$ is the cross-phase.[23] The spectral coherence is defined by $\gamma = |P_{xy}(\omega)|/\sqrt{|P_{xx}(\omega)P_{yy}(\omega)|}$. Because the two floating potential pins ϕ_{f3} and ϕ_{f4} are on the highest plateau and the poloidal distance between them is only 5.2 mm, we choose these two pins to calculate the cross correlation and characterize the SOL turbulence structure. However, in the reversed field case (#171207049), the circuits of pins ϕ_{f3}, ϕ_{f4} and the double probe are damaged, consequently the cross correlation is performed by another two floating potential pins ϕ_{f1} and ϕ_{f2} which are separated by 8.8 mm poloidally. Besides, the electron density and temperature are not available in reversed field in Fig. 6. In Figs. 6, 13, and 18, 2048 sample points ($\sim$1 ms) are used to calculate the discrete Fourier transform of the cross correlation. The CPSD reveals similar radial structure in both the normal and reversed fields. In the normal field, the CPSD increases dramatically when the field line connection length is larger than 200 m, and the high level CPSD is distributed in a large frequency regime (up to 200 kHz). A broadband turbulence below 160 kHz is located in the radial region of $R = 6.057$–6.074 m. When $R = 6.045$–6.055 m, the

CPSD is concentrated in the low frequency turbulence below 40 kHz. When $R < 6.042$ m, the CPSD is distributed in a wider frequency range (up to 200 kHz). In the reversed field, the same radial structure of the CPSD can be found in Fig. 6(f), apart from the slight enlargement of the frequency range of the CPSD. In normal field, the normalized cross-coherence is above 0.8 in the inner half region ($R = 6.057$–6.065 m) of the broadband turbulence, as presented in Fig. 6(a). When the probe continues to move inwards, the high cross-coherence in 60–160 kHz disappears, while only the low frequency turbulence has high cross-coherence. In the radial region of $R = 6.045$–6.054 m, there is a wide frequency region (40–450 kHz) with cross-coherence above 0.8, and the low frequency turbulence also has high cross-coherence. When $R < 6.045$ m, only the low frequency turbulence below 30 kHz has high cross-coherence, except the radial region of $R = 6.037$–6.042 m where the cross-coherence is above 0.6 in the frequency range up to 100 kHz and decreases gradually with the frequency. In the reversed field, the cross-coherence exhibits the same radial structure as the normal field case, but the value is smaller. The cross-phase between ϕ_{f3} and ϕ_{f4} in the normal field is presented in Fig. 6(c), and the cross-phase between ϕ_{f1} and ϕ_{f2} in the reversed field is presented in Fig. 6(g). As illustrated in Fig. 2(b), pin ϕ_{f1} is on the upward side of pin ϕ_{f2}, and pin ϕ_{f3} is on the upward side of pin ϕ_{f4}. The same cross correlation process is performed for ϕ_{f1} vs ϕ_{f2} and ϕ_{f3} vs ϕ_{f4}. The cross-phase is positive for the broadband turbulence in the normal field, but is negative for the broadband turbulence in the reversed field, denoting that the broadband turbulence propagates upwards in the normal field but downwards in
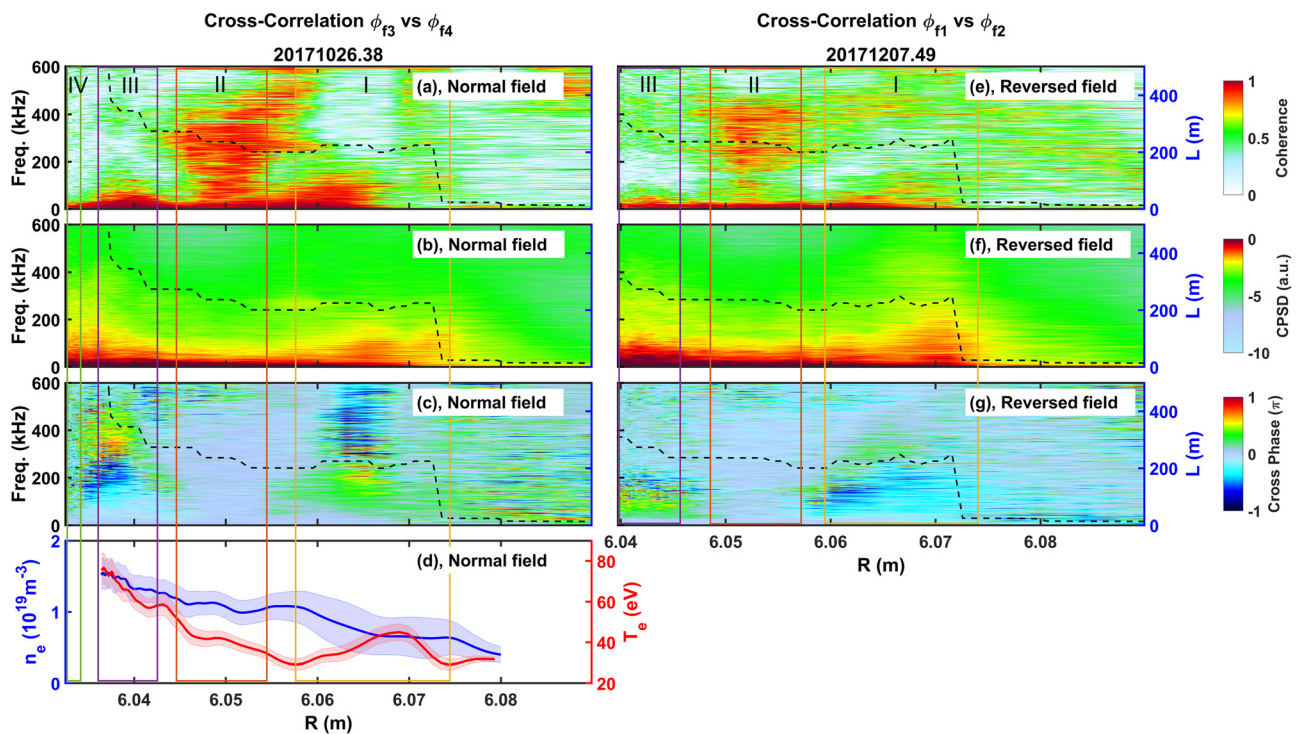

FIG. 6. The cross correlation between two floating potential pins for the normal field (left panels) and reversed field (right panels) in standard configuration. Cross-coherence (a) and (e); CPSD (b) and (f); cross-phase (c) and (g). The profiles of electron density and temperature in normal field are shown in (d). The field line connection length is illustrated in dashed lines. The rectangles denote the radial region of turbulence patterns.

the reversed field, as expected for a $E_r \times B$ dominant poloidal phase velocity. For example, the detailed cross-phase structure can be found in the normal field: the phase of the broadband turbulence in $R = 6.057$–6.072 m is positive, but phase of the turbulence from 30 to 100 kHz with high cross-coherence in $R = 6.037$–6.042 m is negative. The turbulence with high cross-coherence in 40–450 kHz located at $R = 6.045$–6.054 m has a very small cross-phase. Because the probe position of plasma program #20171026.38 is much closer to the LCFS than other discharges in standard and high mirror configurations, the complete radial variations of the SOL turbulence in the island divertor configuration can be illustrated by the plasma program #20171026.38.

As mentioned in Sec. II, the electron temperature and density reach a plateau near the island center along the probe path ($R = 6.067$–6.07 m), where the decrease in the CPSD is observed, as shown in Fig. 6(b). In $R = 6.057$–6.066 m, there is a large radial gradient of electron density, which is consistent with the existence of broadband turbulence in this region. When $R = 6.045$–6.055 m, the variation of electron density is very small, where the low frequency turbulence is dominated. When $R < 6.045$ m, the electron density and temperature increase again with the decreasing R, and a large radial gradient of electron temperature can be found in $R = 6.037$–6.042 m, where the high cross correlation turbulence below 100 kHz appears.

The auto-correlation time of turbulence can be derived from the e-folding time of the auto-correlation function of floating potential. Note that 1000 sample points ($\sim$500 μs) are used to calculate the auto-covariance, and the corresponding auto-correlation function is obtained by taking the average of all the auto-covariance within the given time period (5–10 ms). The raw signal is applied by a high-pass

filter to extract the fluctuations above 1 kHz. The noise level of auto-correlation function is estimated by the significance test with 95% confidence interval and illustrated in the green dashed lines in Fig. 7. Normally the auto-correlation time of turbulence is fitted by the function of $f(t) = e^{-t/\tau_d}$, with $\tau_d \approx 20$ μs for the broadband turbulence dominant region and $\tau_d = 35$–45 μs for the low frequency dominant region, as shown in Figs. 7(a) and 7(b). In Fig. 7(c), the auto-correlation time decreases slightly compared to that in Figs. 7(b) and 7(d), due to the turbulence in 0–100 kHz with high cross-coherence in Fig. 6(a). There is no large difference between the auto-correlation time in normal field and reversed field. However, the fitted curve exhibits some discrepancy with the auto-correlation function in Figs. 7(a) and 7(b). Consequently, a bi-exponential model $f(t) = a_1 e^{-t/\tau_{d1}} + a_2 e^{-t/\tau_{d2}}$ is used to distinct the fast (a_1, τ_{d1}) and slow (a_2, τ_{d2}) decay components. In Figs. 7(e) and 7(f), the fitted curve of bi-exponential model matches the auto-correlation function very well. For the broadband turbulence region, the fast part is the major decay component with $a_1 = 0.62$–0.65 and $\tau_{d1} = 14$–18 μs, while the slow part also play an important role with $a_2 = 0.19$ and $\tau_{d2} = 148$ μs for normal field and $a_2 = 0.16$ and $\tau_{d2} = 209$ μs for reversed field. In Fig. 7(e), the fitted auto-correlation coefficient is about 0.78–0.84 at $\tau_{lag} = 0$, which is smaller than 1. In addition, the curve of auto-correlation function and the fitted line still have significant discrepancy when $\tau_{lag} < 10$ μs, indicating the existence of a much faster decay component than the fitting results of the bi-exponential model. In order to study the relationship between the broadband turbulence and this fast decay component ($\tau_{lag} < 10$ μs), the bi-exponential model is applied to the fluctuation signal in the frequency range from 40 to
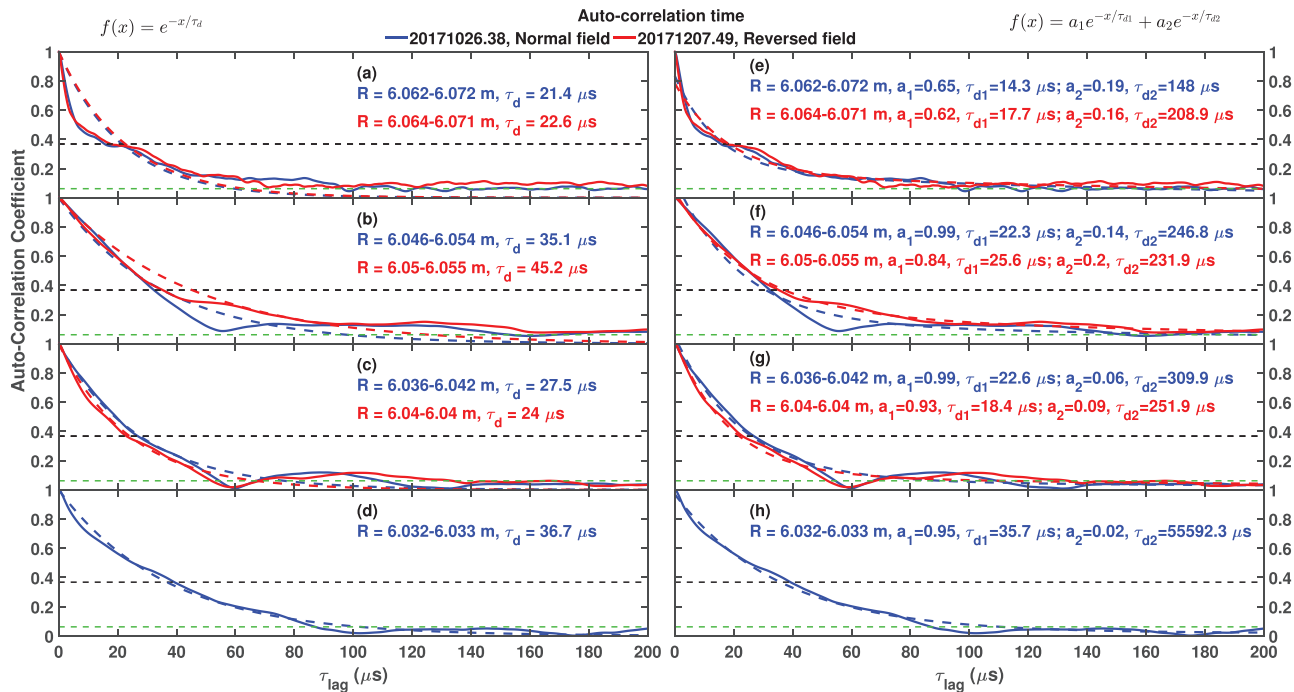

FIG. 7. The auto-correlation function of the floating potential for normal field and reversed field in standard configuration. The auto-correlation time τ_d is fitted by $f(t) = e^{-t/\tau_d}$ and displayed in panels (a)–(d), as illustrated in the dashed lines; in panels (e)–(h), the auto-correlation time is fitted by bi-exponential model $f(t) = a_1 e^{-t/\tau_{d1}} + a_2 e^{-t/\tau_{d2}}$. The green dashed line denotes the noise level.

200 kHz, and the derived fast decay component with $\tau_{d1} = 5\,\mu s$ is consistent with the fast decrease in auto-correlation coefficient when $\tau_{lag} < 10\,\mu s$ in Fig. 7(e), and the slow decay component ($a_2 = 0.03$ and $\tau_{d2} \approx 350\,\mu s$) can be ignored. In consequence, the auto-correlation time τ_{d1} in Fig. 7(e) is contributed by the combination of the broadband turbulence and the low frequency turbulence. For the low frequency turbulence dominant region in Fig. 7(f), the fast decay time is $\tau_{d1} = 22\,\mu s$ and the slow decay time is $\tau_{d2} = 247\,\mu s$, while the weight factor of the slow decay component is $a_2 = 0.14$–0.2. If the bi-exponential model is applied for the fluctuation signal in the frequency range of 5–30 kHz, the derived decay time is $\tau_{d1} = 35$–50 μs which is larger than that in Fig. 7(f). In Figs. 7(g) and 7(h), the weighted factor a_2 is much smaller, indicating that the slow decay component can be ignored compared with the fast decay component. In summary, from the broadband dominant region to the low frequency dominant region, the increase in auto-correlation time is significant.

The turbulence decorrelation rate in the plasma frame can be derived by $\gamma_{decorr}^{pl} = \sqrt{\gamma_{decorr|lab}^2 - (v/l)^2}$, where $\gamma_{decorr|lab}$ is the turbulence decorrelation rate in the laboratory frame and can be estimated by $1/\tau_d$, v is the turbulence velocity, and l is the correlation length.[24] Note that $v = \sqrt{v_\theta^2 + v_r^2}$ is estimated by the turbulence phase velocity, and $l = \sqrt{l_\theta^2 + l_r^2}$ are estimated by the two-point technique with $v_\theta (l_\theta)$ as the poloidal phase velocity (correlation length) and $v_r (l_r)$ as the radial phase velocity (correlation length). For the broadband turbulence (40–200 kHz) in normal field, the auto-correlation time is around 5 μs, correlation length $l \approx 2\,cm$, turbulence velocity

$v \approx 3\,km/s$, therefore the corresponding $\gamma_{decorr}^{pl} = 1.3 \times 10^5\ s^{-1}$. For the low frequency turbulence (5–30 kHz), the auto-correlation time is about 35 μs, $l \approx 8.5\,cm$ and v $\approx 1\,km/s$, so the corresponding $\gamma_{decorr}^{pl} = 2.6 \times 10^4\ s^{-1}$. It should be pointed out that this is a rough estimation of the turbulence decorrelation rate in the plasma frame.

B. Statistical characteristics

In order to study the statistical characteristics of the SOL turbulence in the four radial region in Fig. 6, the poloidal cross-power spectral density $s(k_\theta, f)$, derived from the two-point cross correlation technique,[25,26] is presented in Fig. 8. Since the damage of pins ϕ_{f3} and ϕ_{f4} in the plasma program #171207049, ϕ_{f1} and ϕ_{f2} are used to perform the two-point cross correlation analysis for this discharge, as illustrated in Figs. 8–10. For other discharges, ϕ_{f3} and ϕ_{f4} are used in the two-point cross correlation analysis, as shown in Figs. 8–11, 15–17, 20, and 21. In all the two-point cross correlation analysis, 1024 sample points (500 μs) are used to calculate the discrete Fourier transform, and the number of total points used in each $s(k_\theta, f)$ spectrum in Fig. 8 depends on the given time period (5–10 ms). It should be pointed out that the spectrum $s(k_\theta, f)$ in Fig. 8 is the true cross-power spectral density which reflects the cross-power variation in different radial regions. Another parameter in two-point cross correlation analysis is the normalized CPSD $S(k_\theta, f) = s(k_\theta, f)/\sum_{k_\theta, f} s(k_\theta, f)$ which will be used to calculate other statistical parameters. The two-point cross correlation technique is performed in the frequency range from 1 to 500 kHz, as shown in Figs. 8, 9, 15, 16, and 20. The spectrum
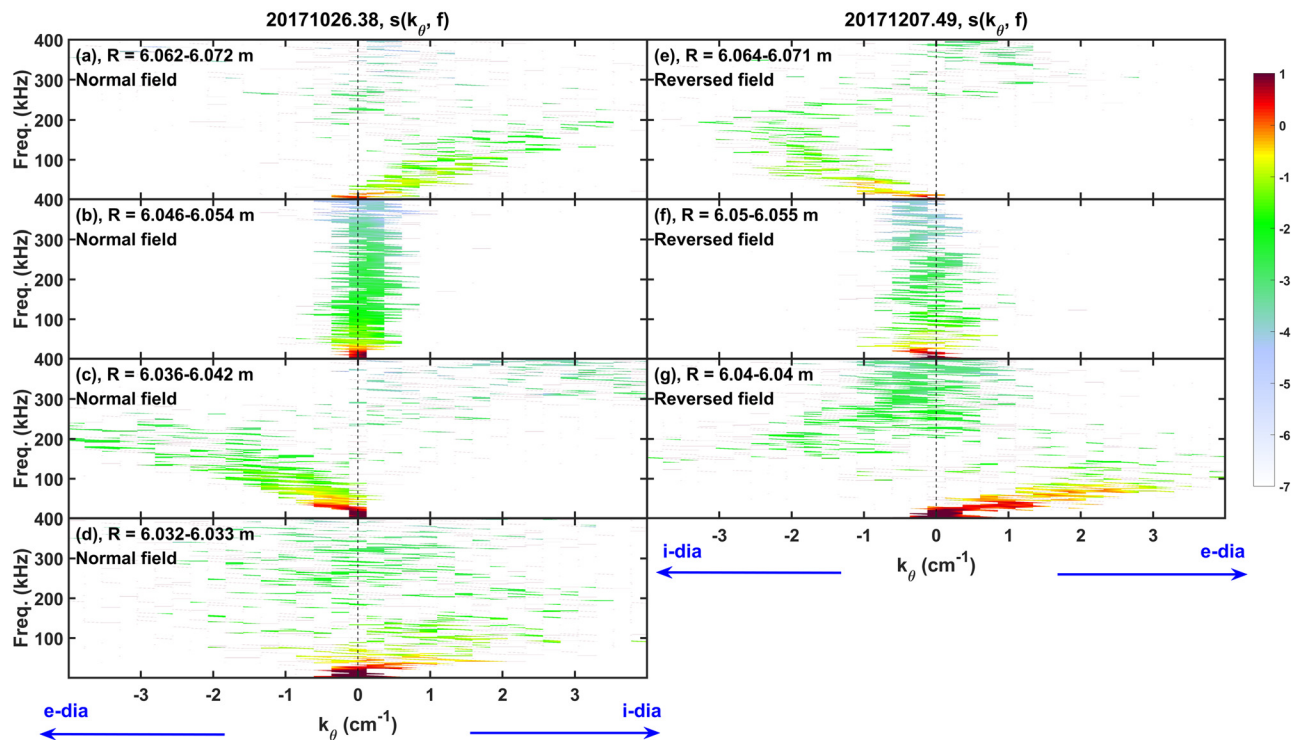

FIG. 8. The poloidal cross-power spectral density $s(k_\theta, f)$ in the standard configuration. The normal field discharge is in panels (a)–(d), while the reversed field discharge is in panels (e)–(g). From the top row to the bottom row, the radial position of probe decreases gradually. The direction of k_θ is illustrated at the bottom panel.
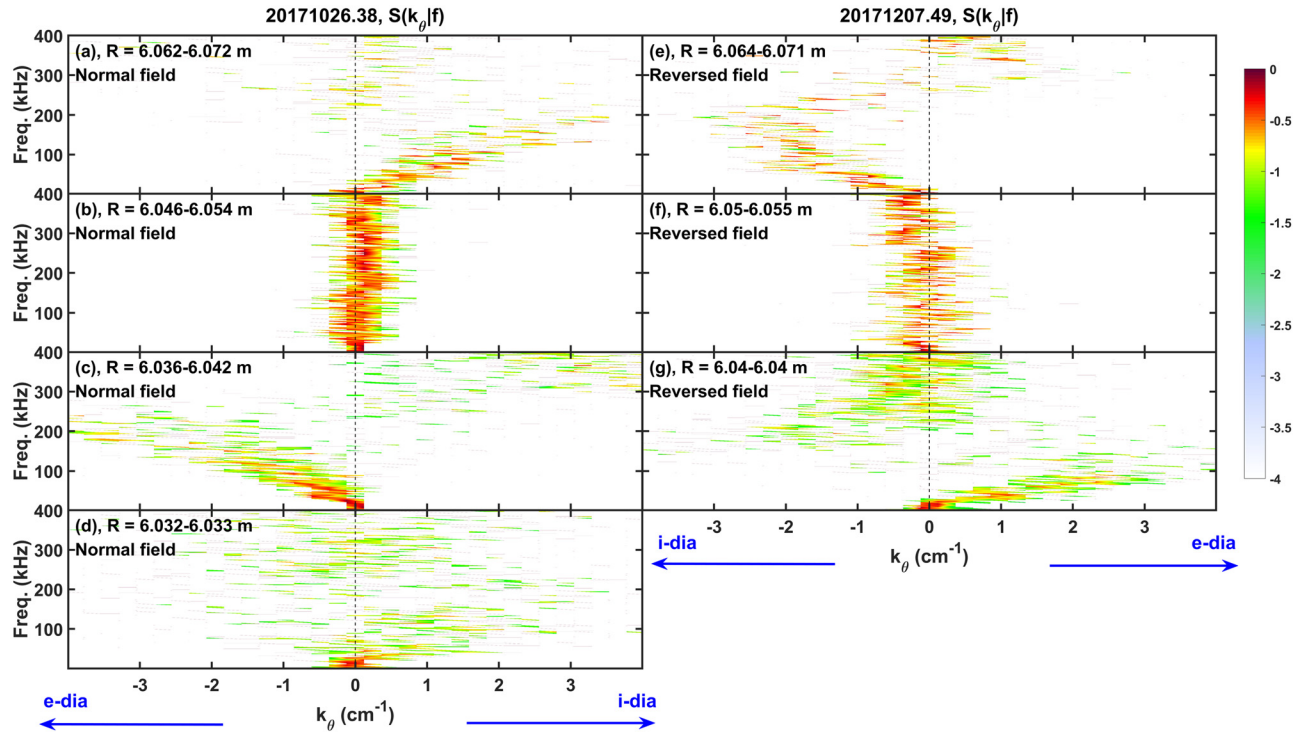
FIG. 9. The conditional poloidal cross-power spectral density $S(k_\theta|f)$ for the standard configuration, with normal field in panels (a)–(d) and reversed field in panels (e)–(g).

$s(k_\theta, f)$ of the broadband turbulence dominant region is shown in Fig. (a), and the turbulence below 160 kHz is located on the side of $k_\theta > 0$, signifying that the broadband turbulence propagates along the direction of ion diamagnetic drift in the laboratory frame. In Fig. 8(b), the spectrum $s(k_\theta, f)$ is symmetrical about $k_\theta = 0$ in a wide frequency range, and most of the cross-power is concentrated in the low frequency region. In Fig. 8(c), the turbulence below 200 kHz propagates along the direction of electron diamagnetic drift in the laboratory frame, and most of the cross-power is located in the frequency below 100 kHz. In Fig. 8(d), at the innermost position of the probe (5 mm outside the LCFS), most of the cross-power $s(k_\theta, f)$ is concentrated in the low frequency turbulence (below 30 kHz) with the poloidal wave number $k_\theta \approx 0$. When the direction of the toroidal magnetic field B_t changes from anti-clockwise (normal field) to clockwise (reversed field), the propagation direction of the turbulence is reversed, i.e., from upwards to downwards for the broadband turbulence [Figs. 8(a) and 8(e)], and from downwards to upwards for the turbulence with high cross-coherence in 0–100 kHz [Figs. 8(c) and 8(g)]. It should be pointed out that the direction of the ion diamagnetic drift is upward in the normal field but downward in the reversed field. Therefore, the broadband turbulence propagates along the direction of ion diamagnetic drift in both the normal and reversed fields, and the turbulence with high cross-coherence in 0–100 kHz propagates along the direction of electron diamagnetic drift in both the normal and reversed fields.

Figure 9 presents the radial evolution of the conditional poloidal cross-power spectral density $S(k_\theta|f) = S(k_\theta, f)/S(f) = S(k_\theta, f)/\sum_{k_\theta} S(k_\theta, f)$ in the SOL of the standard divertor configuration. The

group velocity of the broadband turbulence can be estimated by the slope $V_{group} = 2\pi\Delta f/\Delta k_\theta$ in Figs. 9(a) and 9(e), with $V_{group} \approx 3 \pm 0.6$ km/s for normal field and 3 ± 1.1 km/s for reversed field. Both velocities are along the ion diamagnetic drift direction. Note that this group velocity is estimated by fitting k_{center} and $f(k_{center})$ with a linear function $f = ak_{center} + b$ within the frequency range of the turbulence structure, i.e., 30–160 kHz for the broadband turbulence. Here $k_{center}(f_i) = [\sum_{k_\theta} k_\theta S_{f(i)}(k_\theta|f)]/\sum_{k_\theta} S_{f(i)}(k_\theta|f)$ is the barycenter of $S(k_\theta|f)$ at the frequency slice f_i, where $S_{f(i)}(k_\theta|f)$ is the conditional CPSD at frequency f_i. The error bar of the group velocity is given by fitting. In Figs. 9(c) and 9(g), the group velocity of the turbulence with high cross-coherence in the near SOL is $V_{group} \approx 3.5 \pm 0.7$ km/s for normal field and 1.8 ± 0.6 km/s for reversed field, with their directions along the electron diamagnetic drift. In the low frequency turbulence dominant region, the power spectrum $S(k_\theta|f)$ below 30 kHz is concentrated near $k_\theta = 0$.

When performing the poloidal cross correlation between two probe pins, the poloidal distance d of these two pins should be smaller than half of the interesting turbulence wavelength λ, i.e., $d < \lambda/2$, or $k_\theta < \pi/d = \pi/0.52 = 6$ cm, which is satisfied in Fig. 8.

The poloidal statistical parameters in the standard divertor configuration are illustrated in Fig. 10. During the calculation of each data point of the statistical parameter, 15 360 sample points (7.68 ms) are used to perform the two-point cross correlation. In order to study the statistical parameters in the low frequency turbulence and the broadband turbulence, the raw signals are filtered with a bandpass filter, i.e., 5–30 kHz for the low frequency turbulence, 40–200 kHz for the
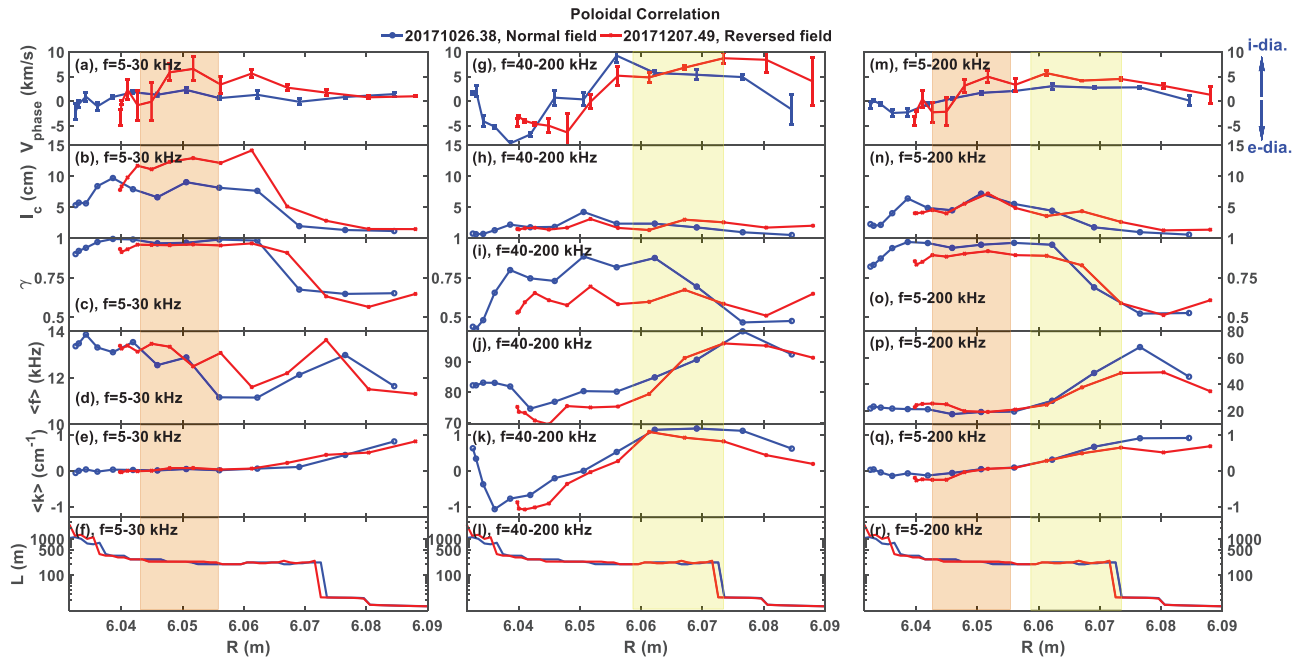
FIG. 10. The poloidal statistical parameters in standard configuration, with the frequency range used in this calculation as 5–30 kHz in the left panels, 40–200 kHz in the middle panels and 5–200 kHz in the right panels. (a), (g), and (m): Turbulence phase velocity, and the error bar denoting the standard deviation; (b), (h), and (n): poloidal correlation length; (c), (i), and (o): correlation coefficient; (d), (j), and (p): averaged frequency; (e), (k), and (q): averaged poloidal wave number; (f), (l), and (r): field line connection length. The positive poloidal phase velocity is in ion diamagnetic drift direction, while the negative phase velocity is in the electron diamagnetic drift direction.
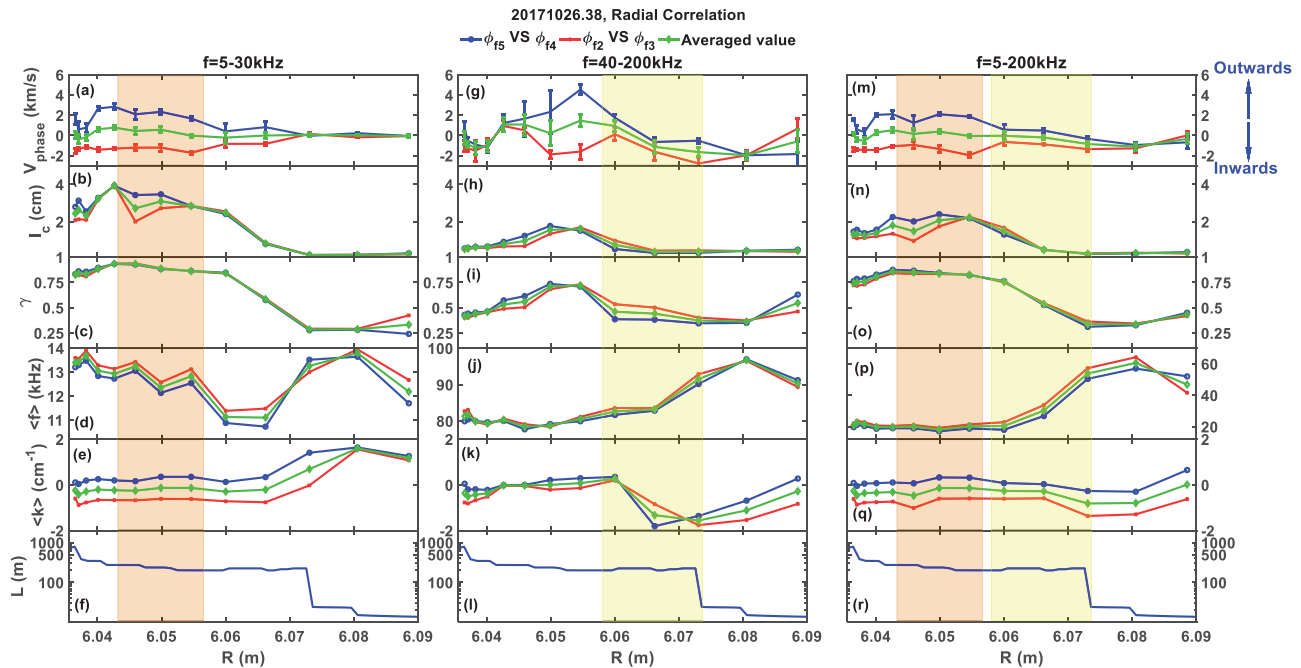

FIG. 11. The radial statistical parameters for plasma program #20171026.38, with the frequency range used in this calculation as 5–30 kHz in the left panels, 40–200 kHz in the middle panels and 5–200 kHz in the right panels. The statements of (a)–(l) are the same as those in Fig. 10, expect that (b), (h), and (n) are the radial correlation length. The positive radial phase velocity in (a), (m) and (m) is outward, while the negative phase velocity is inward. The bule (circle) line signifies the correlation between ϕ_{f5} and ϕ_{f4}, the red (cross) signifies the correlation between ϕ_{f2} and ϕ_{f3}, and the green (diamond) line signifies the averaged value of the former two correlations.

broadband turbulence, and 5–200 kHz for the turbulence with most of the power $s(k_\theta, f)$. Note that the spectra $s(k_\theta, f)$ in these three frequency regions have clear structures, which could reduce the noise level of statistical parameters. For the normal field, from the broadband turbulence dominant region to the low frequency turbulence dominant region, the averaged frequency $\langle f \rangle = \sum f S(f)$ and averaged poloidal wave number $\langle k_\theta \rangle = \sum_f \overline{k}_\theta(f) S(f)$ reduce gradually with decreasing R, where $\overline{k}_\theta(f) = \sum_{k_\theta} k_\theta S(k_\theta|f)$ is the power-averaged dispersion relationship, as presented in Figs. 10(p) and 10(q). As shown in Figs. 10(j) and 10(k), the broadband turbulence ($R = 6.057$–6.074 m) has $\langle f \rangle = 80$–100 kHz and $\langle k_\theta \rangle \approx 1.1$ cm^{-1}; while in Figs. 10(d) and 10(e), the low frequency turbulence ($R = 6.045$–6.055 m) has $\langle f \rangle \approx 12$ kHz and $\langle k_\theta \rangle \approx 0$. In Fig. 10(m), the turbulence poloidal phase velocity defined by $V_{phase} = \sum_{k_\theta, f} 2\pi f S(k_\theta, f)/k_\theta$ has its maximum speed of 3 km/s along the direction of ion diamagnetic drift in the broadband turbulence dominant region, then decreases gradually with decreasing R, and turns to electron diamagnetic drift direction with a speed of -2.5 km/s in the radial region of $R = 6.037$–6.042 m where the turbulence in 0–100 kHz has high cross-coherence. In Fig. 10(g), the turbulence phase velocity of the broadband turbulence calculated from frequency range 40–200 kHz is about $V_{phase} \approx 5$ km/s; while in Fig. 10(a), the phase velocity of the low frequency turbulence calculated from frequency range 5–30 kHz is $V_{phase} = 1$–2 km/s. Note that error bar of phase velocity is estimated by $\sigma = \sigma_1 + \sigma_2$, where $\sigma_1 = \sqrt{\sum_{k_\theta, f}[2\pi f S(k_\theta, f)/k_\theta - v_{phase}]^2/(N-1)}$ is the standard deviation in the two-point cross correlation calculation, where N is the data number of $S(k_\theta, f)$, and σ_2 is the standard deviation among the probe plunges with similar plasma discharge conditions. In Fig. 10(n), the poloidal correlation length $l_{c_\theta} = 1/\langle \sigma_{k\theta} \rangle = 1/\sqrt{\langle \sigma_{k\theta}^2 \rangle}$ increases with the decreasing R, from 1 to 7 cm, with its maximum located in the low frequency turbulence dominant region, where the poloidal wave number spectral width is given by $\langle \sigma_{k_\theta}^2 \rangle = \sum_f \overline{\sigma}_{k_\theta}^2 S(f)$ $= \sum_f S(f) \left\{ \sum_{k_\theta} [k_\theta - \overline{k}_\theta(f)]^2 S(k_\theta|f) \right\}$. As illustrated in Figs. 10(h) and 10(b), the poloidal correlation length is $l_{c_\theta} \approx 2$ cm for the broadband turbulence and 8 cm for the low frequency turbulence. In Fig. 10(o), the correlation coefficient $\gamma = \left\langle \sum_f [\gamma(f) \cdot P_{xy}(f)] / \sum_f P_{xy}(f) \right\rangle$ is from 0.5 to 0.95, where $P_{xy}(f)$ and $\gamma(f)$ are the CPSD and cross-coherence from cross correlation calculation, respectively, and the angle bracket here denotes the ensemble average. As presented in Figs. 10(i) and 10(c), γ in the broadband turbulence is a bit smaller than that of low the frequency turbulence. At the innermost position of the probe, the cross-power $s(k_\theta, f)$ below 30 kHz is much larger than that above 30 kHz, i.e., most of the power is deposited in the low frequency region, with averaged frequency $\langle f \rangle = 20$ kHz, averaged poloidal wave number $\langle k_\theta \rangle \approx 0$, correlation coefficient $\gamma = 0.82$, poloidal correlation length $l_{c\theta} = 2$ cm and phase velocity $V_{phase} = 0.9$ km/s along the direction of electron diamagnetic drift, as shown in the right panels of Fig. 10. It is suggested that the scale of turbulence at the innermost position is smaller than that in the radial region of $R = 6.045$–6.055 m. The statistical parameters in the reversed field agree well with those in the normal field, including the radial evolution and amplitude.

Taylor's hypothesis, an assumption that the turbulence structure past a fixed point can be treated as frozen in the mean flow,[27] holds when the turbulence propagates very rapidly in the plasma frame and its structure propagation speed varies little. In the application of the two-point cross correlation technique in our experiment, the Taylor's hypothesis can be interpreted as follow: the characteristic timescale of turbulence structure should be much larger than the time period of turbulence passing the two probe pins. In our experiment, the poloidal distance between ϕ_{f3} and ϕ_{f4} is 5.2 mm, and the mean flow velocity can be estimated by the turbulence phase velocity which is between 1 and 4 km/s, and the corresponding passing time is $\Delta t_{pass} = 1.3$–5 μs. The turbulence auto-correlation time is $\tau_d = 15$–20 μs, which is much larger than the turbulence passing time, indicating the validation of Taylor's hypothesis in this radial region.

The radial statistical parameters derived from two groups of radially separated floating potential pins ϕ_{f5} vs ϕ_{f4} and ϕ_{f2} vs ϕ_{f3} in the normal field are given in Fig. 11. As illustrated in Fig. 2(b), the radial and poloidal distances between ϕ_{f5} and ϕ_{f4} is the same as those between ϕ_{f2} and ϕ_{f3}. Furthermore, the poloidal direction from ϕ_{f5} and ϕ_{f4} is opposite with that from ϕ_{f2} and ϕ_{f3}. Although the probe head and tips are designed to align the local flux surface, the poloidal propagation of turbulence could affect the radial cross correlation between two radially separated pins, because the eddy shape has a certain size and it is tilted in the poloidal vs radial plane. In consequence, an average between a statistical parameter (such as turbulence phase velocity and wave number) from the correlation between ϕ_{f5} and ϕ_{f4} and that between ϕ_{f2} and ϕ_{f3} could eliminate the poloidal effects and reveal the true radial statistical parameter of turbulence. The radial averaged frequency $\langle f \rangle$ has almost the same radial evolution as the poloidal averaged frequency. The radial correlation coefficient γ also reveals similar radial evolution with the poloidal correlation coefficient, only with a slightly smaller value. The radial correlation length $l_{cr} = 0.2$–2 cm in frequency region 5–200 kHz increases gradually with decreasing R, with its maximum located in the low frequency turbulence dominant region, as illustrated in Fig. 11(n). In Fig. 11(h), the radial correlation length of the broadband turbulence derived from turbulence within 40–200 kHz is $l_{cr} = 0.4$–0.7 cm; while for the low frequency turbulence the radial correlation length derived from turbulence within 5–30 kHz is $l_{cr} = 2.5$–4 cm, as shown in Fig. 11(b). The turbulence radial phase velocity exhibits a large difference between the ϕ_{f5} vs ϕ_{f4} and ϕ_{f2} vs ϕ_{f3} cases, with the former V_{phase} directed outwards in most of the SOL region but the later V_{phase} directed inwards, which indicating the existence of the poloidal propagation component of turbulence in the radial cross correlation between two radially separated pins. Therefore, it is necessary to make an average between the cross-correlations of ϕ_{f5} vs ϕ_{f4} and ϕ_{f2} vs ϕ_{f3}. In Fig. 11(m), the averaged V_{phase} is close to zero in the radial region of $R = 6.06$–6.075 m, and about 0.1–0.4 km/s in the region of $R = 6.045$–6.055 m. In Fig. 11(a), the averaged phase velocity of low frequency turbulence is $V_{phase} \approx 0.5$ km/s and directed outwards; while in Fig. 11(g), the averaged phase velocity of broadband turbulence is $V_{phase} = -1.5$–1 km/s. In the radial region $R = 6.037$–6.042 m where the turbulence within 100 kHz has high cross-coefficient, the radial correlation length is about 1.3 cm which is smaller than that of the low frequency turbulence, and the radial phase velocity reduces to negative value and directed inwards.

For the low frequency turbulence in normal field, the poloidal and radial correlation lengths are about $l_{c\theta} = 8$ and $l_{cr} = 2.5$–4 cm, respectively; and the poloidal and radial phase velocities are about

$V_{phase,\theta} = 1$–2 km/s and $V_{phase,r} = 0.1$–0.4 km/s, respectively. With these parameters, a sketch of the eddy shape and speed are illustrated in Fig. 12. We can see the eddy is elongated, mainly along the local flux surface and tilted slightly. The eddy motion is mainly along the poloidal direction, since the poloidal speed is much larger than the radial speed.

To summarize the characterization of the SOL turbulence in the standard configuration, some common features are discovered, the SOL turbulence can be classified into four patterns according to its frequency domain and propagation property. The first pattern is the broadband turbulence near the magnetic island center along the probe path, propagating along the direction of the ion diamagnetic drift, accompanied by a large gradient of electron density. The second pattern is located on the inner side of the broadband turbulence, with most of the cross-power deposited in the low frequency region (<30 kHz), and the poloidal power spectrum $S(k_\theta|f)$ symmetric about $k_\theta = 0$. The third pattern is located on the inner side of the second one, with a CPSD distributed in a wider frequency range than that in the low frequency turbulence dominant region, and exhibiting a high cross-coherence in 0–100 kHz, propagating along the direction of electron diamagnetic drift. The third pattern turbulence could be related to the gradient of electron temperature because a large gradient of electron temperature is found in the same radial region. The fourth pattern is located in the near SOL (serval millimeter outside the LCFS), with most of the poloidal cross-power $s(k_\theta, f)$ concentrated in the low frequency region (<30 kHz). In contrast to the low frequency dominant turbulence, the broadband turbulence has smaller poloidal correlation length and auto-correlation time, but larger turbulence poloidal phase velocity and averaged poloidal wave number, indicating that the broadband turbulence is mainly driven by small-scale fluctuations, while the low frequency turbulence is driven by large-scale
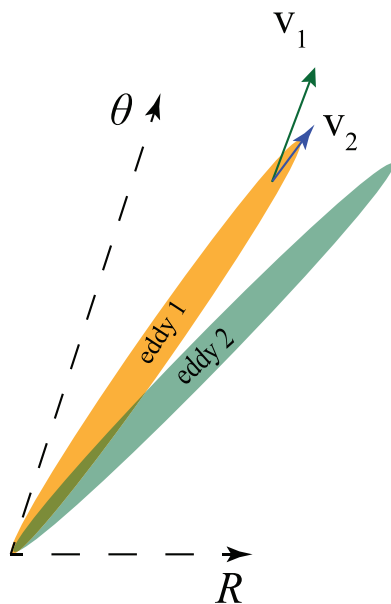

FIG. 12. A simple sketch of the eddy shape by using the statistical parameters of the low frequency turbulence in discharge 20171026.38. The velocities v_1 and v_2 signify the angle range of the eddy speed direction.

fluctuations. Previously the radial transport induced by the SOL turbulence has been discussed in detail.[13] The broadband turbulence from several tens kilo Hz to about 200 kHz contributes to outward heat flux and particle flux. The outward radial transport reduces notably in the low frequency turbulence dominant region on the inner side of this broadband turbulence, but increases in the radial region of the third pattern turbulence. The probability distribution function (PDF) of the ion saturation current obeys the Gaussian distribution in the broadband turbulence region, but has elevated tails between the Gaussian and Laplace distributions in the low frequency turbulence region, indicating the small-scale fluctuations in the broadband turbulence region and the enhancement of large-scale fluctuations in the low frequency turbulence dominant region.[13] The large-scale SOL fluctuations could be referred to as filaments, which has been studied in the SOL of W7-X by using a probe array,[28] demonstrating that these SOL filaments reveal the same properties as the interchange mode and have limited contribution to the radial transport due to their small radial displacement. In this paper, the statistical characteristics of the SOL turbulence are discussed detailed, aiming to give a complete physical image of the SOL turbulence in the island divertor configuration of OP 1.2a. The parameters of the four patterns of the SOL turbulence in normal field of standard divertor configuration are presented in Table I. In the reversed field case, the statistical parameter and propagation properties of the SOL turbulence agree well with those in normal field case, demonstrating the same physical mechanism of turbulence in the SOL.

IV. SOL TURBULENCE IN HIGH MIRROR CONFIGURATION

In this section, a plasma program #20171017.47 in the high mirror configuration is analyzed. The reciprocating probe was plunged twice to measure the SOL turbulence structure in two ECRH power plateaus, with $P_{ECRH} = 1$ and 2.1 MW, respectively. The APSD of floating potential is shown in Figs. 5(f) and 5(g), which has a clear existence of broadband turbulence in the outer SOL and low frequency turbulence in the inner SOL. In addition, the frequency range of the broadband turbulence in high mirror configuration is much wider than that in standard configuration, especially in the 2.1 MW case. As shown in Fig. 13, the poloidal cross correlation of the SOL turbulence in high mirror configuration also exhibits similar radial structure with that in the standard configuration. As shown in Fig. 1(a), the LCFS is located at $R = 6.005$ m, and the innermost position of the reciprocating probe in this discharge is at $R = 6.022$ m, i.e., the probe is 17 mm outside the LCFS. In this case, only the first two SOL turbulence patterns can be observed in high mirror configuration, because the probe doesn't reach the radial region of the last two turbulence patterns. This can be confirmed by the flat profile of n_e and T_e when $R < 6.04$ m, as illustrated in Figs. 13(d) and 13(h), while the third turbulence pattern is accompanied by a large gradient of T_e. Since the magnetic island and the LCFS in high mirror configuration are shifted inward when compared to those in the standard configuration, the locations of the first two SOL turbulence patterns are shifted accompanied by the magnetic island topology. In addition, the CPSD is enhanced significantly in the 2.1 MW case, and the extension of its frequency range is also observed, as shown in Figs. 13(b) and 13(f).

The turbulence auto-correlation time is presented in Fig. 14. In Figs. 14(a)–14(c), we can see the normal fitting $f(t) = e^{-t/\tau_d}$ has large difference with the auto-correlation function. Therefore, we use the

TABLE I. The parameters of four patterns of SOL turbulence in the normal field of the standard divertor configuration.

Turbulence patterns	I	II	III	IV
R	6.057–6.074 m	6.045–6.055 m	6.037–6.042 m	<6.037 m
Dominant frequency	40–160 kHz	0–30 kHz	0–100 kHz	0–30 kHz
Turbulence propagation	Ion diamagnetic drift	$S(k_\theta, f)$ symmetric about $k_\theta = 0$	Electron diamagnetic drift	$k_\theta \approx 0$
Poloidal correlation length	1–2 cm	6–9 cm	4–6 cm	2 cm
Radial correlation length	0.3–0.6 cm	2.5–4 cm	1.3 cm	…

bi-exponential model $f(t) = a_1 e^{-t/\tau_{d1}} + a_2 e^{-t/\tau_{d2}}$ to distinguish the fast and slow decay components. For the broadband turbulence region in Fig. 14(d), the fast decay time τ_{d1} is 5.5 and 2.6 μs for the 1 MW and 2.1 MW cases, while the slow decay time τ_{d2} is 112 and 130 μs for the 1 and 2.1 MW cases. The weighted factor $a_1/a_2 = 0.61/0.34$ and $0.5/0.49$ corresponding to 1 and 2.1 MW cases. If compared with the results from standard configuration in Fig. 7(e), the fitting curves match the auto-correlation function very well when $\tau_{lag} < 10\,\mu$s in high mirror configuration, and the corresponding fast decay time τ_{d1} is close to that derived from the 40–200 kHz turbulence in standard configuration. This observation may be related to the wide distribution of turbulence in frequency space and the enhancement of power spectral density in high frequency region, which can be seen in Figs. 5 and 13. For the low frequency turbulence dominant region in Fig. 14(e), the fast decay time increases to about 30 μs, and the slow decay time increases to 164 and 192 μs for the 1 and 2.1 MW cases. The ratio of weighted factor $a_1/a_2 = 0.69/0.33$ and $0.51/0.52$ for the 1

and 2.1 MW cases. In contrast with the results of standard configuration in Fig. 7(f), the fast decay time in high mirror configuration is a bit larger for the second turbulence pattern, but the corresponding weighted factor a_1 decreases significantly. In both the broadband and low frequency turbulence dominant regions, the slow decay component plays an important role in the turbulence decay time since its weighted factor $a_2 = 0.33$–0.52. Furthermore, when the heating power raises from 1 MW to 2.1 MW, the fast decay time decreases, while the slow decay time increases, indicating the existence of long-time correlation and enhancement of the related large-scale fluctuations in higher heating power case.

The poloidal cross correlation spectrum $s(k_\theta, f)$ for the two patterns of the SOL turbulence is shown in Fig. 15. The broadband turbulence is located in the radial region of $R = 6.048$–6.068 m, and the $s(k_\theta, f)$ is illustrated in Figs. 15(a) and 15(d). In the two ECRH power cases, the turbulence below 200 kHz is located on the side of $k_\theta > 0$, signifying that the broadband turbulence propagates along the
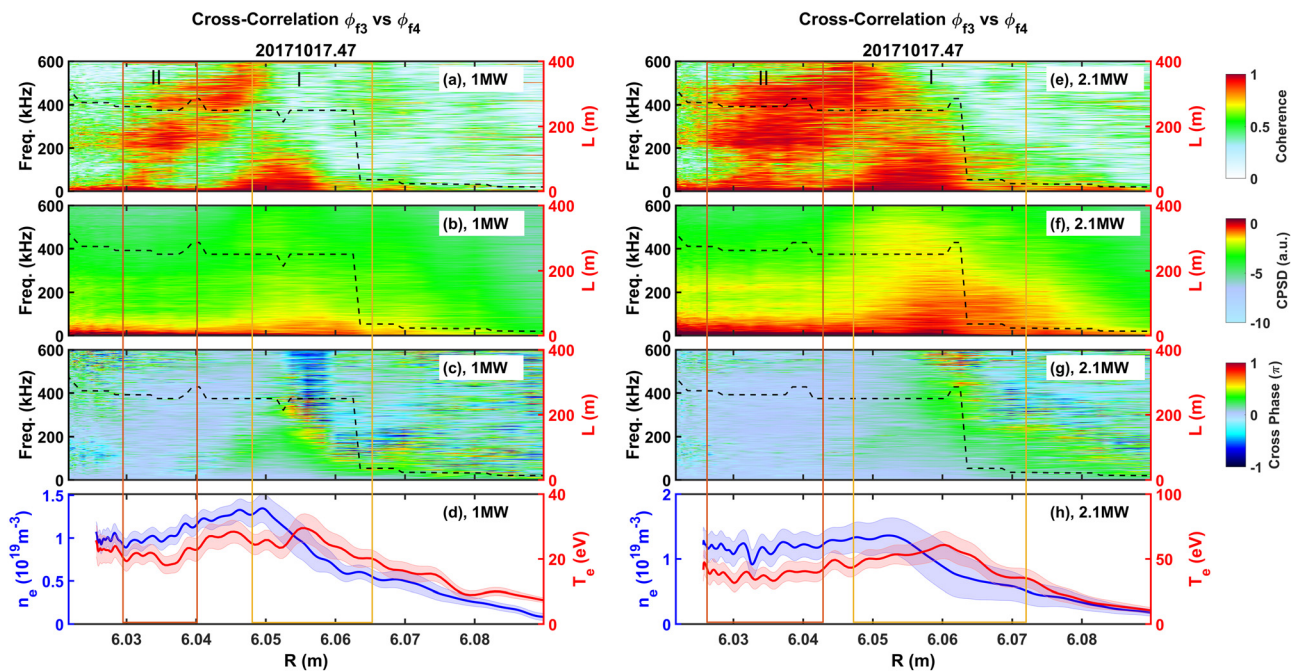

FIG. 13. The cross correlation between two floating potential pins in high mirror configuration. Cross-coherence (a) and (e); CPSD (b) and (f); cross-phase (c) and (g). The profiles of electron density and temperature are shown in (d) and (h). The field line connection length is shown in the dashed lines. The rectangles denote the radial region of turbulence patterns.
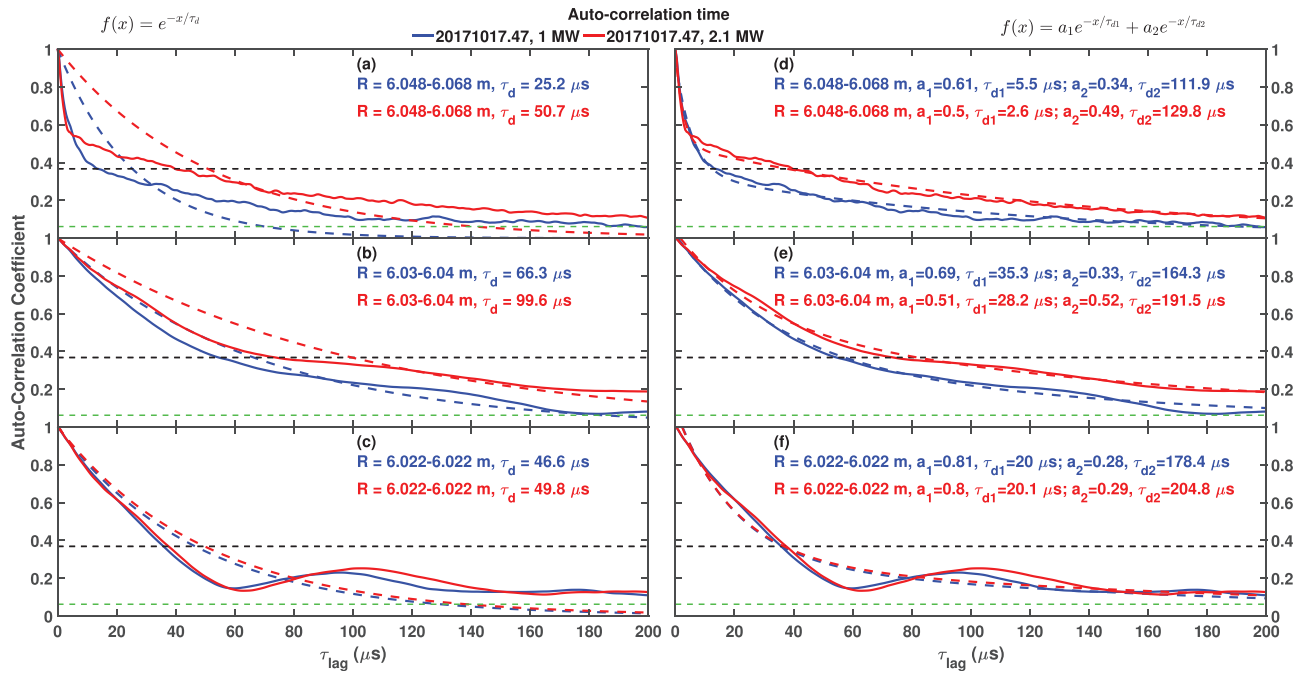
FIG. 14. The auto-correlation function of the floating potential in high mirror configuration. The auto-correlation time τ_d is fitted by $f(t) = e^{-t/\tau_d}$ and displayed in panels (a)–(c), as illustrated in the dashed lines; in panels (d)–(f), the auto-correlation time is fitted by bi-exponential model $f(t) = a_1 e^{-t/\tau_{d1}} + a_2 e^{-t/\tau_{d2}}$. The green dashed line denotes the noise level.
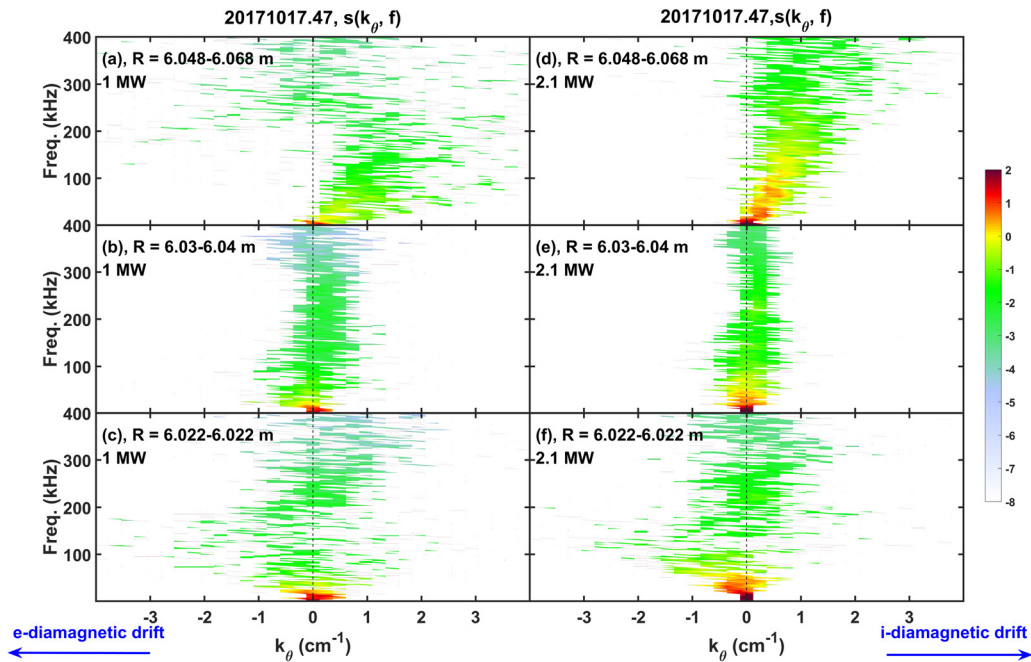

FIG. 15. The poloidal cross-power spectral density $s(k_\theta, f)$ of high mirror configuration. The ECRH power of left panels (a)–(c) is 1 MW, and 2.1 MW for the right panels (d)–(f). From the top row to the bottom row, the radial position of the probe decreases gradually. The positive poloidal wave number k_θ denotes the direction of ion diamagnetic drift, while the negative k_θ denotes the direction of the electron diamagnetic drift.

direction of ion diamagnetic drift in the laboratory frame. In addition, the poloidal cross-power spectral density in 2.1 MW case is larger than that in 1 MW case. The dispersion relationship of the broadband turbulence is clear in the poloidal conditional spectrum $S(k_\theta|f)$, as shown in Figs. 16(a) and 16(d). The group velocity in the laboratory frame of this broadband turbulence can be derived by $V_{group} = 2\pi\Delta f/\Delta k_\theta$, with 4.3 ± 1.5 and 12.7 ± 1.5 km/s in the direction of ion diamagnetic drift corresponding to the 1 and 2.1 MW cases, respectively. The mean value of the poloidal electric drift velocity in the radial region of $R = 6.048$–6.068 m is $V_{E\times B} = E_r/B_\varphi \approx 2.3 \pm 1$ and 4.5 ± 0.5 km/s in the direction of ion diamagnetic drift for the 1 and 2.1 MW cases. In consequence, the group velocity of the broadband turbulence in the plasma frame is $V_{group} - V_{E\times B} \approx 2 \pm 2.5$ and 7.2 ± 2 km/s in the ion diamagnetic drift direction for 1 and 2.1 MW cases, respectively. In Figs. 15(b) and 15(e), the poloidal spectrum $s(k_\theta, f)$ is almost symmetric about $k_\theta = 0$, and most of the spectral power is deposited in the low frequency turbulence. At the innermost point of the probe, as listed in Figs. 15(c) and 15(f), $s(k_\theta, f)$ is concentrated in the low frequency turbulence below 30 kHz. These two patterns of SOL turbulence are consistent with those observed in the standard divertor configuration.

In the SOL plasma of limiter configuration on W7-X, the spectra $s(k_\theta, f)$ and $S(k_\theta|f)$ are mainly distributed on the side of $k_\theta > 0$, i.e., propagating along the direction of ion diamagnetic drift in the near SOL (16 mm outside the LCFS).[14] In the standard and high mirror configurations, the SOL turbulence reveals four patterns of structure, which suggests that the SOL turbulence is affected significantly by the edge magnetic topology in W7-X.

The poloidal statistical parameters in high mirror configuration is presented in Fig. 17, and exhibits similar radial evolution with those in the standard configuration. In the 1 MW case, the broadband

turbulence in radial region $R > 6.05$ m has the following statistical parameters: when derived from the fluctuations in 5–200 kHz, turbulence poloidal phase velocity $V_{phase} = 1.5$–3 km/s, poloidal correlation length $l_{c\theta} = 1$–6 cm, correlation coefficient $\gamma = 0.5$–0.97, averaged frequency $\langle f \rangle = 20$–45 kHz, and averaged poloidal wave number $\langle k_\theta \rangle = 0.4$–1.5 cm^{-1}; when derived from the fluctuations in 40–200 kHz, $V_{phase} = 2.5$–8.5 km/s, $l_{c\theta} = 0.6$–3.5 cm, $\gamma = 0.45$–0.87, $\langle f \rangle \approx 90$ kHz, and $\langle k_\theta \rangle = 0.7$–1.8 cm^{-1}. In the 2.1 MW case, the statistical parameters of the broadband turbulence are as follows: when derived from the fluctuations in 5–200 kHz, $V_{phase} = 2$–7.8 km/s, $l_{c\theta} = 2$–8 cm, $\gamma = 0.7$–0.98, $\langle f \rangle = 20$–70 kHz, and $\langle k_\theta \rangle = 0.05$–0.9 cm^{-1}; when derived from the fluctuations in 40–200 kHz, $V_{phase} = 6$–14 km/s, $l_{c\theta} = 2$–6 cm, $\gamma = 0.7$–0.93, $\langle f \rangle = 80$–110 kHz, and $\langle k_\theta \rangle = 0.37$–1.3 cm^{-1}. If compared with the results derived from fluctuations in 5–200 kHz, the statistical parameters derived from fluctuations in 40–200 kHz fluctuations directly reflect the properties of the broadband turbulence in the radial range of $R = 6.048$–6.072 m. For example, the poloidal phase velocities in Fig. 17(g) are much closer to the group velocity of broadband turbulence in Fig. 16(d) than the phase velocity in Fig. 17(m). With the raise of ECRH heating power, significant increases of V_{phase}, $l_{c\theta}$, $\langle f \rangle$ are observed, and the decrease in $\langle k_\theta \rangle$ is also obvious. In the low frequency turbulence dominant region, the statistical parameters are as follows: when derived from the fluctuations in 5–30 kHz, $V_{phase} = -1.7$–1 km/s, $l_{c\theta} = 5$–6.7 cm, $\gamma = 0.92$–0.97, $\langle f \rangle \approx 11$ kHz, and $\langle k_\theta \rangle \approx 0$ cm^{-1} for the 1 MW case; $V_{phase} = -1$–1 km/s, $l_{c\theta} = 7$–8 cm, $\gamma = 0.98$, $\langle f \rangle \approx 11$ kHz, and $\langle k_\theta \rangle \approx 0$ cm^{-1} for the 2.1 MW case. A strong enhancement of the poloidal correlation length due to the increase in the ECRH heating power is observed, indicating larger scale of turbulence in higher heating power case.
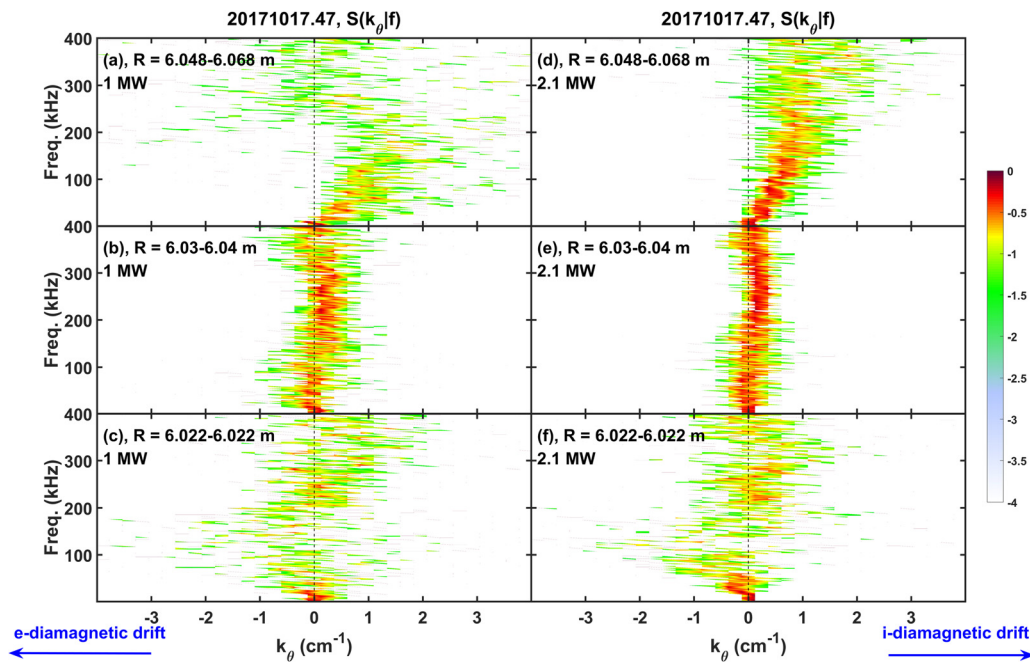

FIG. 16. The conditional poloidal cross-power spectral density $S(k_\theta|f)$ for high mirror configuration, with 1 MW ECRH power for panels (a)–(c) and 2.1 MW for panels (d)–(f).
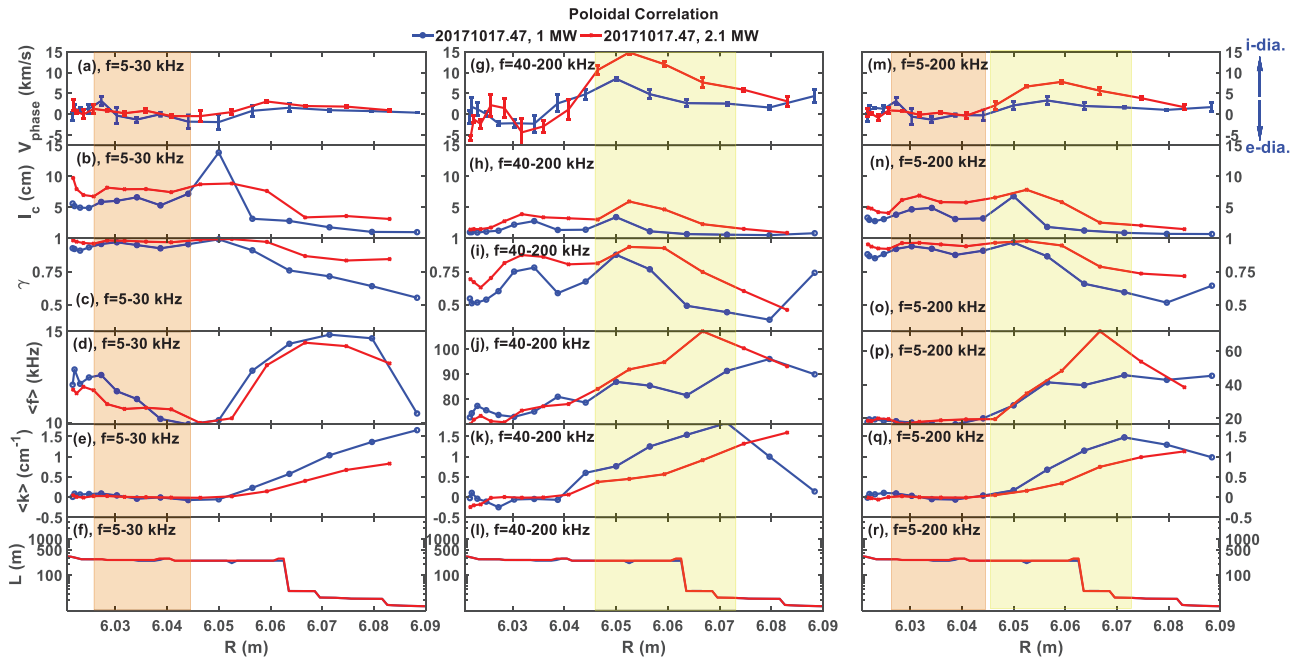
FIG. 17. The poloidal statistical parameters for the high mirror configuration, with the frequency range used in this calculation as 5–30 kHz in the left panels, 40–200 kHz in the middle panels, and 5–200 kHz in the right panels. The statements of (a)–(l) are the same as those in Fig. 10.

In both the standard and high mirror configurations, the statistical characteristics of the SOL turbulence exhibit the same radial evolution, which confirms that the SOL turbulence could be classified into four patterns, as discussed in Sec. III. In the limiter configuration on W7-X, the phase velocity in the SOL is from -0.5 to 0.9 km/s and the poloidal correlation length is from 0.4 to 1 cm.[14] In consequence, the turbulence phase velocity and the poloidal correlation length in the divertor configuration are an order of magnitude larger than those in the limiter configuration on W7-X.

V. SOL TURBULENCE IN HIGH IOTA CONFIGURATION

The SOL magnetic island is very narrow in high iota configuration, with the LCFS located at $R = 6.001$ m, as illustrated in Fig. 1. Besides, a global oscillation with a frequency about 200 Hz is observed by some diagnostics covering the core and edge plasma in high iota configuration, which is also measured by the reciprocating probe in the SOL, as illustrated in the large amplitude oscillations of floating potential in Fig. 18(a). Due to the small size of the SOL island and the large global oscillation, the SOL turbulence in high iota configuration is quite different with that in the standard and high mirror configurations. As shown in Fig. 18(a), the signal of floating potential is very weak in the far SOL ($R > 6.023$ m), starts to increase when $R < 6.018$ m, and further increases when $R < 6.005$ m. The APSD of the floating potential is enhanced with the decreasing major radius R, as presented in Fig. 18(b). Note that the highlighted horizontal bands are caused by the 200 Hz global oscillations. The cross correlation between ϕ_{f3} and ϕ_{f4} is displayed in Figs. 18(d)–18(f). When the connection length increases to about 100 m, the CPSD increases gradually with the decreasing R. When $R < 6.005$ m, the CPSD is further enhanced not only in the amplitude, but also distributed in a

wider frequency space. As shown in Fig. 18(d), only the low frequency (below 20 kHz) turbulence has high cross-coherence in the radial region of $R > 6.01$ m. In the near SOL ($R < 6.05$ m), the frequency range with high cross-coherence is much wider and expands up to 100 kHz. In the region with high cross-coherence, the cross-phase is positive and the value is very small.

The turbulence auto-correlation time in high iota configuration is shown in Fig. 19 with four radial positions. The turbulence auto-correlation time τ_d from fitting equation $f(t) = e^{-t/\tau_d}$ is 17.3, 15.7, 27.9, and 29.3 μs corresponding to four radial regions labeled in Figs. 19(a)–19(d), respectively. However, the fitting curves have some difference with the auto-correlation function, especially in the small τ_{lag} region. With bi-exponential model $f(t) = a_1 e^{-t/\tau_{d1}} + a_2 e^{-t/\tau_{d2}}$, the fitting curves match the auto-correlation function very well, as shown in the right panels of Fig. 19. In Fig. 19(f), the fast decay component with $\tau_{d1} = 4.3$ μs and slow decay component with $\tau_{d2} = 54.2$ μs are observed when $R = 6.011$–6.015 m, with the corresponding weighted factor $a_1/a_2 = 0.59/0.37$. In the near SOL, as shown in Fig. 19(g), the fast decay time $\tau_{d1} = 24.7$ μs while the contribution from slow decay component is much weaker. Around the LCFS, the auto-correlation time is $\tau_{d1}/\tau_{d2} = 15.7$ μs/107 μs, and the weighted factor is $a_1/a_2 = 0.62/0.28$.

The poloidal cross-power spectral density $s(k_\theta, f)$ and $S(k_\theta|f)$ in high iota configuration, derived from two floating potential pins ϕ_{f3} and ϕ_{f4}, are presented in Fig. 20. In the far SOL, the poloidal power spectrum $S(k_\theta, f)$ is very small compared with that in the near SOL, and there is no clear dispersion relationship. In the radial region $R = 6.001$–6.005 m, the poloidal power spectrum $s(k_\theta, f)$ increases significantly in 0–400 kHz, especially for the low frequency turbulence (below 50 kHz) which has a symmetrical distribution of $S(k_\theta|f)$ about
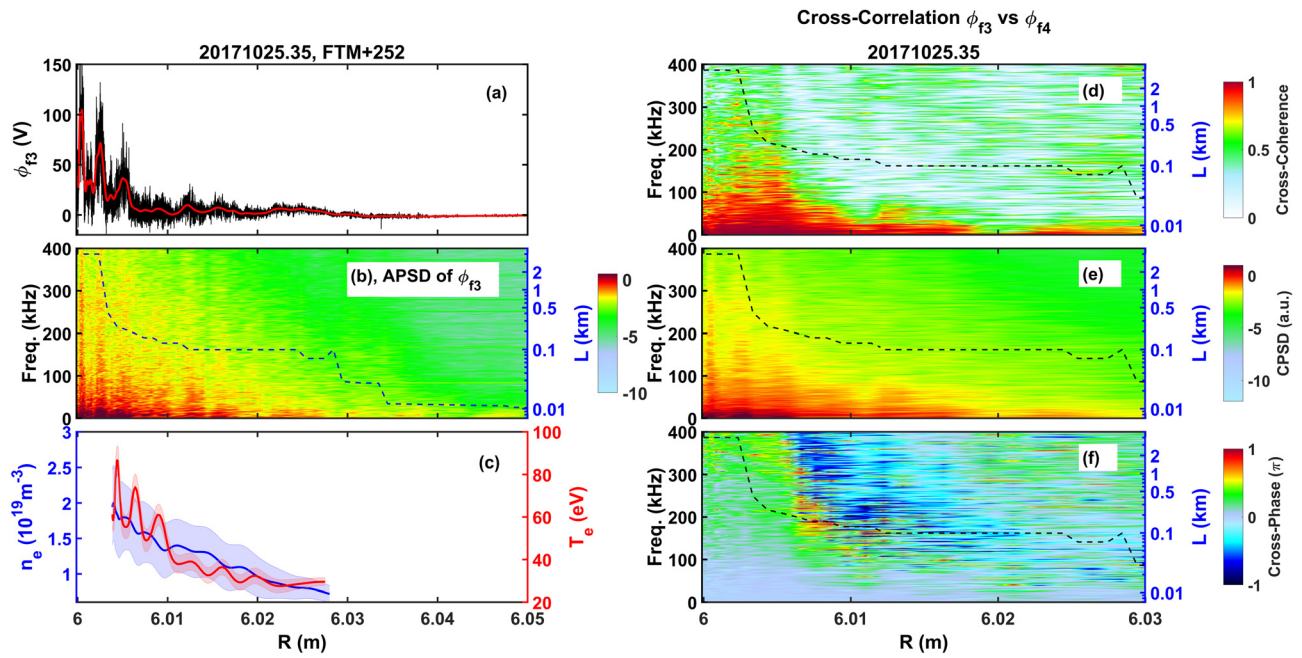
FIG. 18. The turbulence power spectra in the high iota configuration. (a) The fluctuation level of the floating potential; (b) the APSD of the floating potential ϕ_{f3}; (c) the electron density and temperature profiles measured by probe; the cross correlation between two floating potential pins (ϕ_{f3} and ϕ_{f4}), with the cross-coherence (d), the CPSD (e) and the cross-phase (f). The field line connection length is shown in the black dashed lines.
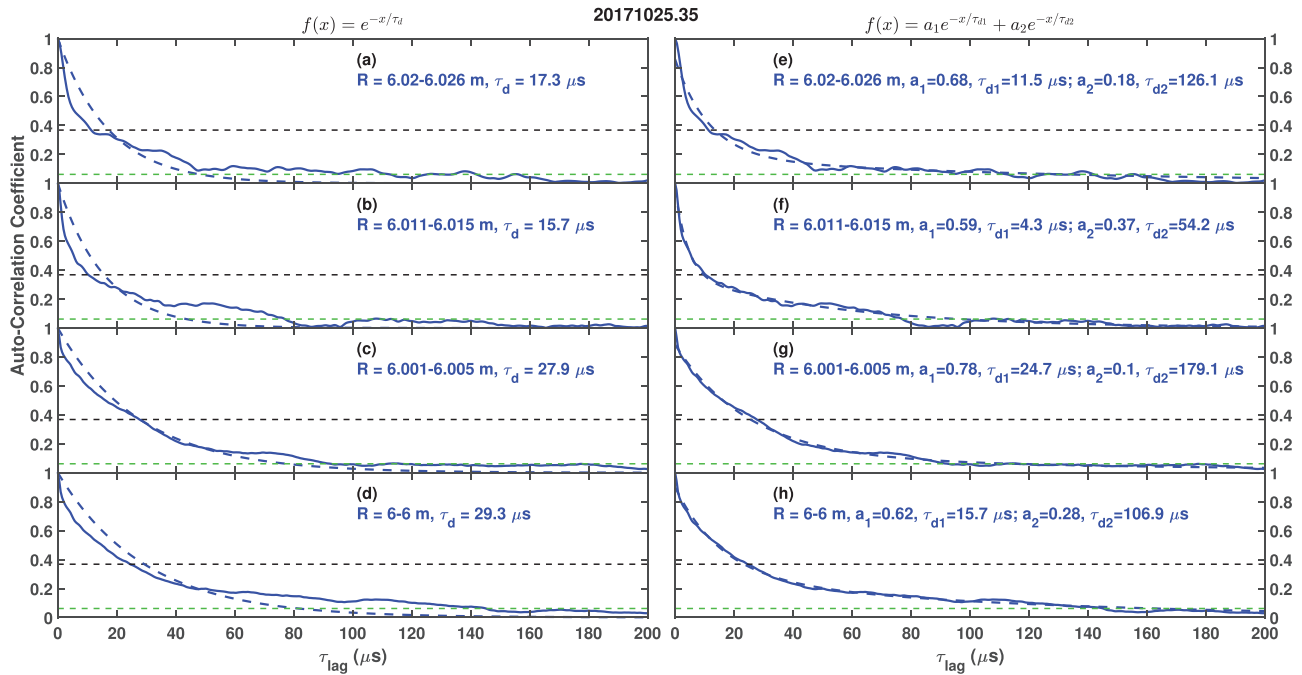

FIG. 19. The auto-correlation function of the floating potential in high iota configuration. The auto-correlation time τ_d is fitted by $f(t) = e^{-t/\tau_d}$ and displayed in panels (a)–(c), as illustrated in the dashed lines; in panels (d)–(f), the auto-correlation time is fitted by bi-exponential model $f(t) = a_1 e^{-t/\tau_{d1}} + a_2 e^{-t/\tau_{d2}}$. The green dashed line denotes the noise level.
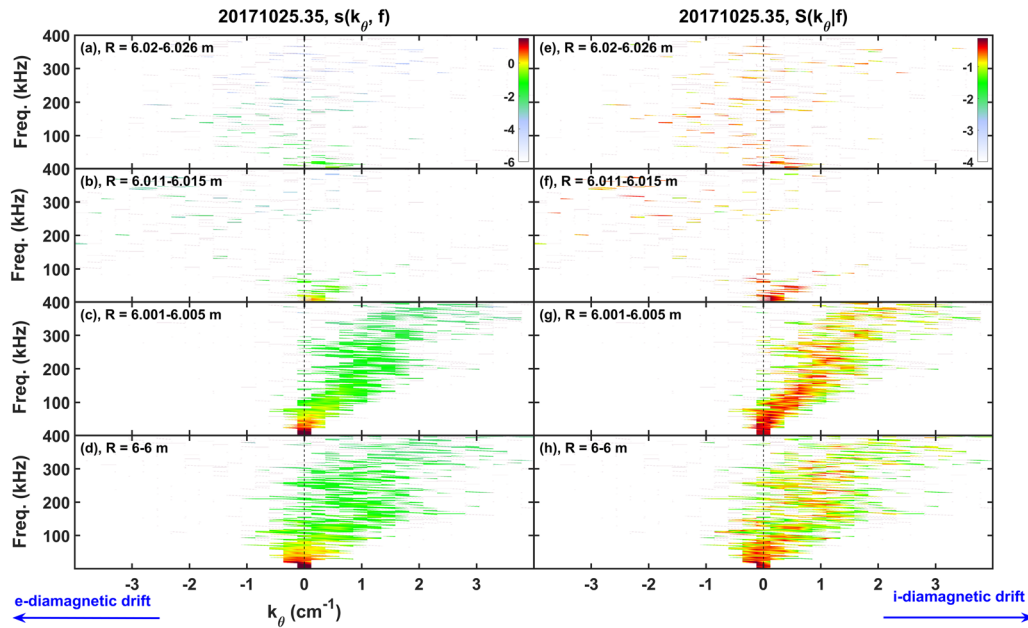
FIG. 20. The poloidal cross-power spectral density $s(k_\theta, f)$ (a)–(d) and the poloidal conditional cross-power spectral density $S(k_\theta|f)$ (e)–(h) in high iota configuration. The direction of k_θ is illustrated at the bottom panels.

$k_\theta = 0$. The turbulence in the frequency range above 50 kHz reveals a clear dispersion relationship, propagating along the direction of the ion diamagnetic drift with a group velocity $V_{group} = 2\pi\Delta f/\Delta k_\theta \approx 8 \pm 0.7$ km/s in the laboratory frame, as illustrated in Figs. 20(c) and 20(g). If the poloidal electric drift velocity $V_{E\times B} \approx 2 \pm 1$ km/s in the ion diamagnetic drift is taken into account, the propagation velocity of this turbulence structure is about 6 ± 1.7 km/s along the ion diamagnetic drift direction in the plasma frame. At the innermost point of the probe (around LCFS), most of the power $S(k_\theta, f)$ is deposited in the frequency below 80 kHz, and the turbulence above 80 kHz also propagates along the ion diamagnetic drift direction.

The statistical parameters in high iota configuration are presented in Fig. 21. In $R = 6.018$–6.03 m, the statistical parameters derived from fluctuations in 5–200 kHz are as follows: averaged frequency $\langle f \rangle \approx 40$ kHz, averaged poloidal wave number $\langle k_\theta \rangle = 0.07$–$0.11$ cm^{-1}, correlation coefficient $\gamma = 0.6$–0.7, poloidal correlation length $l_{c\theta} \approx 1.2$ cm, turbulence phase velocity 0–1 km/s. From $R = 6.017$ to 6.008 m, significant increases are observed in the statistical parameters derived from fluctuations in 5–200 kHz: $\langle k_\theta \rangle$ from 0.1 to 0.25 cm^{-1}, γ from 0.7 to 0.87, V_{phase} from 1.5 to 3.5 km/s. While the averaged frequency $\langle f \rangle$ decreases slightly in this radial region, and the poloidal correlation length $l_{c\theta} \approx 1.3$ cm. From $R = 6.005$ m to 6.001 m, V_{phase} and $\langle k_\theta \rangle$ decrease significantly and they are close to zero near the LCFS ($R = 6.001$ m); $\langle f \rangle$ decreases to about 24 kHz; γ and $l_{c\theta}$ increase remarkably and reach their maxima at $R = 6.003$ m, then decrease gradually with decreasing R. As illustrated in Figs. 18 and 20, the frequency range with high APSD and CPSD extends to over 200 kHz when $R < 6.005$ m. In this radial region, the poloidal phase velocity derived from fluctuations in 40–200 kHz is higher than that from fluctuations in 5–200 kHz, with $V_{phase} = 6$–10 km/s which is close

to the group velocity in Fig. 20(g). The corresponding poloidal correlation length is $l_{c\theta} = 2.5$–3.5 cm. As shown in Fig. 4, the connection length starts to increases greatly when $R < 6.008$ m, and the electron temperature and density also increase sharply in this
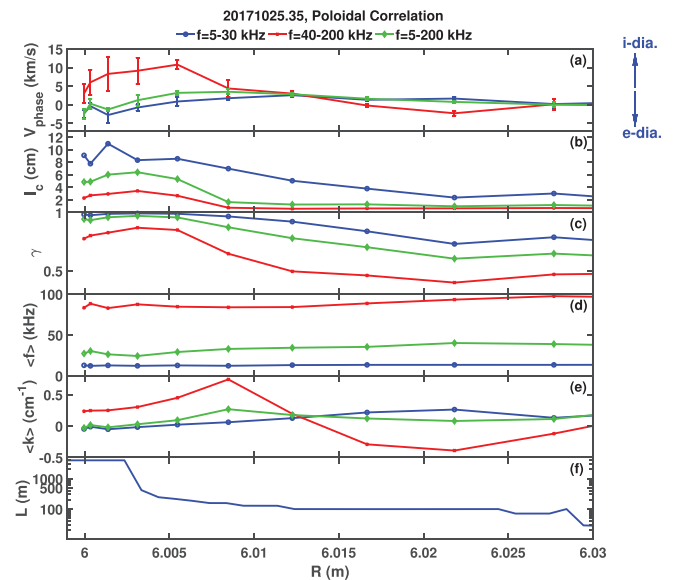

FIG. 21. The poloidal statistical parameters in the high iota configuration, with the frequency range used in this calculation as 5–30 kHz in the blue curves, 40–200 kHz in the red curves and 5–200 kHz in the green curves. (a) Turbulence phase velocity, and the error bar denoting the standard deviation; (b) correlation length; (c) correlation coefficient; (d) averaged frequency; (e) averaged wave number; (f) field line connection length.

region, which is consistent with the observation of the clear turbulence dispersion relationship in Figs. 20(c) and 20(g).

VI. SUMMARY

The statistical characteristics of the SOL turbulence in the first divertor plasma operation of W7-X have been measured by the reciprocating probe, exhibiting a strong dependence on the magnetic configuration, toroidal field direction and ECRH heating power. Since the standard divertor and high mirror configurations have similar SOL magnetic island structure along the path of reciprocating probe, they have some common features on the radial structure of the SOL turbulence and the corresponding statistical parameters. According to the turbulence frequency domain and propagation property, the SOL turbulence in standard and high mirror configurations can be classified into four patterns. The first pattern is the broadband turbulence near the magnetic island center along the probe path, propagating along the direction of ion diamagnetic drift, accompanied by a large gradient of electron density. The second pattern is located on the inner side of the broadband turbulence, with most of the cross-power deposited in the low frequency region (<30 kHz), and the poloidal power spectrum $s(k_\theta, f)$ symmetric about $k_\theta = 0$. The third pattern is located on the inner side of the second one, with a CPSD distributed in a wider frequency range than that in the low frequency turbulence dominant region, and exhibiting a high cross-coherence in 0–100 kHz, propagating along the direction of the electron diamagnetic drift. The third pattern turbulence could be related to the gradient of electron temperature because a large gradient of electron temperature is found in the same radial region. The fourth pattern is located in the near SOL (serval millimeter outside the LCFS), with most of the poloidal power spectrum $s(k_\theta, f)$ concentrated in the low frequency region (<30 kHz), and $k_\theta \approx 0$.

The turbulence statistical parameters have been derived by using the two-point cross correlation technique. In the standard configuration, the typical statistical parameters of the four patterns turbulence are as below: the first pattern (broadband) turbulence has a turbulence phase velocity around 4–10 km/s along the ion diamagnetic drift direction, and a poloidal correlation length around 1–3 cm; the second pattern (low frequency dominant) turbulence has much smaller turbulence phase velocity and larger poloidal correlation length around 6–12 cm; in the radial region of the third pattern turbulence, the turbulence phase velocity turns to the direction of electron diamagnetic drift, and the poloidal correlation length is around 4–6 cm which is smaller than that of the second pattern turbulence.

The turbulence auto-correlation time is about 5 μs for the broadband turbulence and over 25 μs for the low frequency turbulence. Besides, the turbulence auto-correlation time can be decomposed into fast and slow decay components in the regions of the first and second turbulence patterns. In contrast to the low frequency dominant turbulence, the broadband turbulence has smaller poloidal correlation length and auto-correlation time, but larger turbulence phase velocity and averaged poloidal number, indicating that the broadband turbulence is mainly driven by small-scale fluctuations, while the low frequency turbulence is driven by large-scale fluctuations. In the radial region of the third pattern turbulence, the decreases of turbulence auto-correlation time and poloidal correlation length indicate that the turbulence in 0–100 kHz with high cross-coherence contributes significantly to the turbulence behavior. Compared to the standard

configuration, the locations of the SOL turbulence patterns in high mirror configuration are shifted according to the magnetic topology.

The effect of the ECRH heating power on the broadband turbulence is obvious. The turbulence power spectral density, phase velocity, poloidal correlation length and averaged frequency can be increased significantly by raising the ECRH heating power, but the averaged poloidal wave number decreases significantly at the same time. When the toroidal magnetic field changes from anti-clockwise direction viewed from top (normal field) to clockwise direction (reversed field), the SOL turbulence propagation direction is reversed in the space but remains in the same diamagnetic drift direction. The radial statistical parameters are analyzed by two groups of radially separated floating potential pins in the standard divertor configuration, with a relatively small radial correlation length for the broadband turbulence, and a value up to 3 cm for the low frequency turbulence. An outward propagation of the low frequency turbulence is observed.

In the high iota configuration, turbulence in the far SOL is very weak due to the narrow SOL island, and no clear dispersion relationship can be found in the poloidal cross correlation spectrum. In the near SOL, the turbulence is enhanced significantly, and exhibits a clear turbulence propagation in the direction of ion diamagnetic drift. The poloidal correlation length is about 2–3 cm in the near SOL. Because of the much narrower width of the SOL magnetic island in high iota configuration when compared to the other two configurations, the four-pattern SOL turbulence structure is not observed. This confirms that the SOL turbulence and the statistical parameters in W7-X are affected significantly by the local magnetic topology.

DATA AVAILABILITY

The data that support the findings of this study are available from the corresponding author upon reasonable request.

REFERENCES

[1]E. J. Doyle, W. A. Houlberg, Y. Kamada, V. Mukhovatov, T. H. Osborne, A. Polevoi, G. Bateman, J. W. Connor, J. G. Cordey, T. Fujita, X. Garbet, T. S. Hahm, L. D. Horton, A. E. Hubbard, F. Imbeaux, F. Jenko, J. E. Kinsey, Y. Kishimoto, J. Li, T. C. Luce, Y. Martin, M. Ossipenko, V. Parail, A. Peeters, T. L. Rhodes, J. E. Rice, C. M. Roach, V. Rozhansky, F. Ryter, G. Saibene, R. Sartori, A. C. C. Sips, J. A. Snipes, M. Sugihara, E. J. Synakowski, H. Takenaga, T. Takizuka, K. Thomsen, M. R. Wade, H. R. Wilson, ITPA Transport Physics Topical Group, ITPA Confinement Database and Modelling Topical Group, and ITPA Pedestal and Edge Topical Group, Nucl. Fusion **47**, S18 (2007).
[2]W. Horton, Rev. Mod. Phys. **71**, 735 (1999).

[3]G. R. Tynan, A. Fujisawa, and G. McKee, Plasma Phys. Controlled Fusion **51**, 113001 (2009).

[4]M. Endler, H. Niedermeyer, L. Giannone, E. Holzhauer, A. Rudyj, G. Theimer, and N. Tsois, Nucl. Fusion **35**, 1307 (1995).

[5]G. D. Conway, B. Scott, J. Schirmer, M. Reich, A. Kendl, and ASDEX Upgrade Team, Plasma Phys. Controlled Fusion **47**, 1165 (2005).

[6]S. J. Zweben, R. J. Maqueda, D. P. Stotler, A. Keesee, J. Boedo, C. E. Bush, S. M. Kaye, B. LeBlanc, J. L. Lowrance, V. J. Mastrocola, R. Maingi, N. Nishino, G. Renda, D. W. Swain, J. B. Wilgen, and NSTX Team, Nucl. Fusion **44**, 134 (2004).

[7]G. R. McKee, C. Fenzi, R. J. Fonck, and M. Jakubowski, Rev. Sci. Instrum. **74**, 2014 (2003).

[8]S. C. Liu, Y. Liang, P. Drews, A. Kramer-Flecken, X. Han, D. Nicolai, G. Satheeswaran, N. C. Wang, J. Q. Cai, A. Charl, J. Cosfeld, G. Fuchert, Y. Gao, J. Geiger, O. Grulke, M. Henkel, M. Hirsch, U. Hoefel, K. P. Hollfeld, D. Hoschen, C. Killer, A. Knieps, R. Konig, O. Neubauer, E. Pasch, K. Rahbarnia, M. Rack, N. Sandri, S. Sereda, B. Schweer, E. H. Wang, Y. L. Wei, G. Weir, T. Windisch, and W7-X Team, Nucl. Fusion **58**, 046002 (2018).

[9]A. Kramer-Flecken, X. Han, T. Windisch, J. Cosfeld, P. Drews, G. Fuchert, J. Geiger, O. Grulke, C. Killer, A. Knieps, Y. Liang, S. Liu, M. Rack, and W7-X Team, Plasma Phys. Controlled Fusion **61**, 054003 (2019).

[10]C. Killer, O. Grulke, P. Drews, Y. Gao, M. Jakubowski, A. Knieps, D. Nicolai, H. Niemann, A. P. Sitjes, G. Satheeswaran, and W7-X Team, Nucl. Fusion **59**, 086013 (2019).

[11]P. Drews, C. Killer, J. Cosfeld, A. Knieps, S. Brezinsek, M. Jakubowski, C. Brandt, S. Bozhenkov, A. Dinklage, J. Cai, M. Endler, K. Hammond, M. Henkel, Y. Gao, J. Geiger, O. Grulke, D. Hoschen, R. Konig, A. Kramer-Flecken, Y. Liang, Y. Li, S. Liu, H. Niemann, D. Nicolai, O. Neubauer, U. Neuner, M. Rack, K. Rahbarnia, L. Rudischhauser, N. Sandri, G. Satheeswaran, S. Schilling, H. Thomsen, T. Windisch, S. Sereda, and W7-X Team, Nucl. Mater. Energy **19**, 179 (2019).

[12]X. Han, A. Krämer-Flecken, T. Windisch, M. Hirsch, G. Fuchert, J. Geiger, O. Grulke, S. Liu, and K. Rahbarnia, Nucl. Fusion **60**, 016011 (2020).

[13]S. C. Liu, Y. Liang, P. Drews, C. Killer, A. Knieps, G. S. Xu, H. Q. Wang, N. Yan, X. Han, D. Hoschen, A. Kramer-Flecken, D. Nicolai, G. Satheeswaran, K. Hammond, J. Q. Cai, A. Charl, J. Cosfeld, G. Fuchert, Y. Gao, J. Geiger, O. Grulke, M. Henkel, M. Hirsch, U. Hoefel, R. Konig, Y. Li, O. Neubauer, E. Pasch, K. Rahbarnia, M. Rack, N. Sandri, S. Sereda, B. Schweer, E. H. Wang, S. Xu, X. Gao, and W7-X Team, Nucl. Fusion **59**, 066001 (2019).

[14]S. C. Liu, Y. Liang, P. Drews, A. Kramer-Flecken, X. Han, D. Nicolai, G. Satheeswaran, N. C. Wang, J. Q. Cai, A. Charl, J. Cosfeld, Y. Gao, O. Grulke, M. Henkel, K. P. Hollfeld, C. Killer, A. Knieps, R. Konig, O. Neubauer, M. Rack, N. Sandri, S. Sereda, B. Schweer, E. H. Wang, Y. L. Wei, and W7-X Team, Phys. Plasmas **25**, 072502 (2018).

[15]T. S. Pedersen, M. Otte, S. Lazerson, P. Helander, S. Bozhenkov, C. Biedermann, T. Klinger, R. C. Wolf, H. S. Bosch, and W7-X Team, Nat. Commun. **7**, 13493 (2016).

[16]J. Geiger, C. D. Beidler, Y. Feng, H. Maassberg, N. B. Marushchenko, and Y. Turkin, Plasma Phys. Controlled Fusion **57**, 014004 (2015).

[17]S. A. Bozhenkov, J. Geiger, M. Grahl, J. Kisslinger, A. Werner, and R. C. Wolf, Fusion Eng. Des. **88**, 2997 (2013).

[18]M. Grahl, J. Svensson, A. Werner, T. Andreeva, S. Bozhenkov, M. Drevlak, J. Geiger, M. Krychowiak, Y. Turkin, and W7-X Team, IEEE Trans. Plasma Sci. **46**, 1114 (2018).

[19]M. Grahl, T. Bluhm, M. Grun, C. Hennig, A. Holtz, J. G. Krom, G. Kuhner, H. Laqua, M. Lewerentz, H. Riemann, A. Spring, A. Werner, and W7-X Team, Fusion Eng. Des. **123**, 1015 (2017).

[20]G. Satheeswaran, K. P. Hollfeld, P. Drews, D. Nicolai, O. Neubauer, B. Schweer, and O. Grulke, Fusion Eng. Des. **123**, 699 (2017).

[21]D. Nicolai, V. Borsuk, P. Drews, O. Grulke, K. P. Hollfeld, T. Krings, Y. Liang, C. Linsmeier, O. Neubauer, G. Satheeswaran, B. Schweer, G. Offermanns, and W7-X Team, Fusion Eng. Des. **123**, 960 (2017).

[22]I. H. Hutchinson, *Principles of Plasma Diagnostics* (Cambridge University Press, Cambridge, New York, 2002).

[23]E. J. Powers, Nucl. Fusion **14**, 749 (1974).

[24]G. R. Tynan, M. Xu, P. H. Diamond, J. A. Boedo, I. Cziegler, N. Fedorczak, P. Manz, K. Miki, S. Thakur, L. Schmitz, L. Zeng, E. J. Doyle, G. M. McKee, Z. Yan, G. S. Xu, B. N. Wan, H. Q. Wang, H. Y. Guo, J. Dong, K. Zhao, J. Cheng, W. Y. Hong, and L. W. Yan, Nucl. Fusion **53**, 073053 (2013).

[25]J. M. Beall, Y. C. Kim, and E. J. Powers, J. Appl. Phys. **53**, 3933 (1982).

[26]S. J. Levinson, J. M. Beall, E. J. Powers, and R. D. Bengtson, Nucl. Fusion **24**, 527 (1984).

[27]G. I. Taylor, Proc. R. Soc. London, Ser. A **164**, 476 (1938).

[28]C. Killer, B. Shanahan, O. Grulke, M. Endler, K. Hammond, L. Rudischhauser, and W.-X. Team, Plasma Phys. Controlled Fusion **62**, 085003 (2020).